JOURNAL OF GEOPHYSICAL RESEARCH: PLANETS, VOL. 118, 487–513, doi:10.1029/2012JE004151, 2013

Mineralogy and morphology of geologic units at Libya Montes, Mars: Ancient aqueously derived outcrops, mafic flows, fluvial features, and impacts

Janice L. Bishop,[1,2] Daniela Tirsch,[3] Livio L. Tornabene,[4] Ralf Jaumann,[3,5] Alfred S. McEwen,[6] Patrick C. McGuire,[7,8] Anouck Ody,[9] Francois Poulet,[9] Roger N. Clark,[10] Mario Parente,[11] Nancy K. McKeown,[12] John F. Mustard,[13] Scott L. Murchie,[8] Joana Voigt,[3] Zeynep Aydin,[3] Marlene Bamberg,[3] Andreas Petau,[3] Gregory Michael,[5] Frank P. Seelos,[8] Christopher D. Hash,[8] Gregg A. Swayze,[10] and Gerhard Neukum[5]

Received 31 May 2012; revised 18 October 2012; accepted 1 November 2012; published 31 March 2013.

[1] There is ample evidence of both ancient and long-lasting fluvial activity and chemical alteration in the Libya Montes region south of Isidis Basin. The region hosts Noachian to Amazonian aged surface rocks with extensive outcrops of olivine- and pyroxene-bearing material. Libya Montes also features surface outcrops and/or deposits hosting Fe/Mg-smectite, Fe/Mg-smectite mixed with carbonate and/or other Fe/Mg-rich phyllosilicates, and Al-smectite. These units likely formed through chemical alteration connected with hydrothermal activity resulting from the formation of the Isidis Basin and/or the pervasive fluvial activity throughout this region. The morphology and stratigraphy of the aqueous and mafic minerals are described using High Resolution Imaging Science Experiment and High Resolution Stereo Camera derived digital terrain models. Analyses of the Compact Reconnaissance Imaging Spectrometer for Mars spectra show variations in the chemistry of the Fe/Mg-smectite from nontronite-like exposures with spectral features near 2.29 and 2.4 μm more consistent with $Fe_2^{3+}OH$ groups in the mineral structure, and saponite-like outcrops with spectral features near 2.31 and 2.38 μm characteristic of $Mg_3^{2+}OH$ groups. These Fe/Mg-smectite bearing materials also have bands near 1.9 μm due to H_2O and near 2.5 μm that could be due to the smectite, other phyllosilicates, and carbonates. All regions exhibiting carbonate features near 3.4–3.5 μm also have features consistent with the presence of olivine and Fe/Mg-smectite, indicating that the carbonate signatures occur in rocks likely containing a mixture of these minerals. The Al-smectite-bearing rocks have bands near 1.41, 1.91, and 2.19 μm that are more consistent with beidellite than other Al-phyllosilicates, indicating a higher-temperature or diagenetically processed origin for this material. Our interpretation of the geologic history of this region is that ancient Noachian basaltic crustal materials experienced extensive aqueous alteration at the time of the Isidis impact, during which the montes were also formed, followed by emplacement of a rough olivine-rich lava or melt, and finally the smooth pyroxene-bearing caprock unit.

All Supporting Information may be found in the online version of this article.

[1]Carl Sagan Center, The SETI Institute, Mountain View, California, USA.
[2]Exobiology Branch, NASA-Ames Research Center, Moffett Field, California, USA.
[3]Institute of Planetary Research, German Aerospace Center (DLR), Berlin, Germany.
[4]University of Western Ontario, London, ON, Canada.
[5]Institute of Geological Sciences, Freie Universitaet Berlin, Berlin, Germany.
[6]Lunar and Planetary Laboratory, University of Arizona, Tucson, Arizona, USA.
[7]Department of Chemical Engineering, West Virginia University, Morgantown, West Virginia, USA.
[8]Applied Physics Laboratory, Laurel, Maryland, USA.
[9]Institut d'Astrophysique Spatial, IAS, Orsay Cedex, France.
[10]U.S. Geological Survey, Denver, Colorado, USA.
[11]Department of Electrical and Computer Engineering, University of Massachusetts, Amherst, Massachusetts, USA.
[12]Department of Physical Sciences, Grant MacEwan University, Edmonton Alberta, Canada.
[13]Department of Geological Sciences, Brown University, Providence, Rhode Island, USA.

Corresponding author: J. L. Bishop, Carl Sagan Center, The SETI Institute, Mountain View, CA 94043, USA. (jbishop@seti.org)

©2012. American Geophysical Union. All Rights Reserved. 2169-9097/13/2012JE004151

Citation: Bishop, J. L., et al. (2013), Mineralogy and morphology of geologic units at Libya Montes, Mars: Ancient aqueously derived outcrops, mafic flows, fluvial features, and impacts, *J. Geophys. Res. Planets*, *118*, 487–513, doi:10.1029/2012JE004151.

1. Introduction

[2] Libya Montes (Figure 1) lies at the border of Isidis Planitia (impact basin) to the north and Terra Tyrrhena (ancient highlands) to the south, with Syrtis Major Planum (shield volcano) to the west; this is a region greatly modified by impact, volcanic, tectonic, aeolian, and fluvial processes [*Scott and Tanaka*, 1986; *Crumpler and Tanaka*, 2003; *Erkeling et al*., 2010; *Jaumann et al*., 2010]. Libya Montes and the southern Isidis region host dense valley networks that incise into terrain dating from the Noachian, Hesperian and Amazonian periods [*Crumpler and Tanaka*, 2003; *Mustard et al*., 2007; *Tornabene et al*., 2008; *Erkeling et al*., 2010; *Jaumann et al*., 2010]. *Ivanov et al*. [2012] describe an impact-dominated episode for the Isidis region from the Noachian to ~3.8 Ga, followed by an episode dominated by volcanic and fluvial/glacial activities (~3.8–2.8 Ga). Surface thermophysical inertia measurements have shown that parts of this region are particularly dusty, especially toward the east [*Murphy et al*., 2007; *Tornabene et al*., 2008], which confounds mineral composition determinations using remote spectral data sets. However, this region still contains extensive and relatively dust-free surface outcrops of olivine- and pyroxene-bearing lithologies identified using data from Observatoire pour la Minéralogie, L'Eau, les Glaces et l'Activité (OMEGA) [*Mustard et al*., 2007; *Ody et al*., 2012] and from the Thermal Emission Spectrometer/Thermal Emission Imaging System (TES/THEMIS) [*Tornabene et al*., 2008]. Surface exposures of olivine and pyroxene at Libya Montes appear to be spectrally, morphologically, and stratigraphically similar to those in Nili Fossae to the northwest of Isidis Basin [e.g., *Tornabene et al*., 2008; *Mustard et al*., 2009]. The olivine-rich unit has been proposed to be impact melts created and emplaced as a consequence of the Isidis basin-forming event [*Mustard et al*., 2007], a nearly globally distributed layer deposited by a mega-impact event [*Edwards and Christensen*, 2011], primitive picritic lavas originating from the Syrtis Major plume or other sources in the southern highlands that postdate the formation of Isidis Basin [*Tornabene et al*., 2008], or basaltic lavas that may predate the Isidis impact that originated from a magmatic source distinct from the source that generated the majority of basaltic materials in the Syrtis Major region [*Hoefen et al*., 2003; *Hamilton and Christensen*, 2005]. Fe/Mg-phyllosilicates as well as Al-phyllosilicates and carbonates were recently reported in the Libya Montes region [*Bishop et al*., 2010], although they are less exposed in surface outcrops compared to those observed at Nili Fossae [*Ehlmann et al*., 2008, 2009].

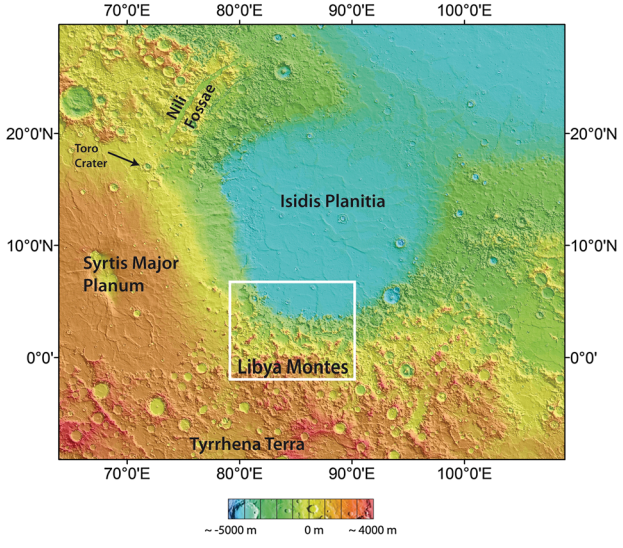

Figure 1. Map of Libya Montes region on MOLA elevation. Libya Montes and other nearby locations are noted.

[3] The study site for this project includes southern Isidis Planitia and western and central Libya Montes where the dust cover is generally lower [see *Murphy et al*., 2007] and mineral exposures are resolved by Compact Reconnaissance Imaging Spectrometer for Mars (CRISM) (Figure 1). Massifs from Isidis were disrupted by Syrtis lavas in most directions around the basin; Libya Montes is an area where these massifs are still present and uncovered [*Wichman and Schultz*, 1989]. This study involves coordinated analyses of multiple data sets. OMEGA images [*Bibring et al*., 2005] provide mineralogical context for the Libya Montes region compared to nearby regions. 5°×5° mosaics of CRISM multispectral mapping data provide additional mineralogical context across the study site while High Resolution Stereo Camera (HRSC) [*Neukum and Jaumann*, 2004] and Context imager (CTX) [*Malin et al*., 2010] data provide geologic context across the study site. Targeted CRISM images [*Murchie et al*., 2009] and High Resolution Imaging Science Experiment (HiRISE) images [*McEwen et al*., 2010] provide detailed mineralogical and morphological information at individual sites, respectively. Mars Orbiter Laser Altimeter (MOLA), HRSC, and HiRISE provide topographic data. Previously published results from TES and THEMIS are also considered [*Tornabene et al*., 2008].

[4] With this study, we seek to understand the geologic history of this region, especially the role of aqueous alteration. Thus, we characterize the phyllosilicate-bearing units in detail in order to understand their composition, morphology, age, and association with local and regional geologic processes. We are also investigating the location and nature of carbonate and its association with phyllosilicates and other minerals in addition to evaluating the widespread olivine-bearing and pyroxene-bearing units in order to determine their relative ages and stratigraphic relationships to the minerals formed by aqueous alteration.

2. Methods

2.1. CRISM Images and Spectral Data

2.1.1. CRISM Hyperspectral Targeted Data

[5] The Compact Reconnaissance Imaging Spectrometer for Mars collects ~10 km wide images from 0.4 to 3.9 μm at ~18 m/pixel in the full resolution targeted (FRT) mode and at ~36 m/pixel in the half-resolution short or long mode [*Murchie et al*., 2009]. CRISM TRR3 images (calibration level 3) that were used for this study include several improvements relative to calibration version 2: (i) a more robust correction for pixel-to-pixel response nonuniformity (flat field correction), (ii) an improved correction for the effects of atmospheric water vapor in the ground calibration optical path, and (iii) correction for the effects of slight observation-to-observation irreproducibility in the viewing geometry of the inflight calibration reference that affected the shape of the ~1 μm absorption common to Fe-bearing phases [*Seelos*, 2011]. In addition, calibration version 3 employs a custom hyperspectral data filtering procedure that is applied to the Planetary Data System (PDS)-delivered *I*/*F* data. The filtering procedure includes a robust approach to systematic noise reduction that is applied to both the short-wavelength (S) 0.4–1 μm and long-wavelength (L) 1–3.9 μm detector data, and an iterative kernel filter applied to the L detector data that is based on a formal statistical outlier test and leverages the hyperspectral character of the data and the high degree of redundancy of adjacent pixels to identify and correct stochastic noise. Both the S and L image cubes were calibrated and evaluated for each observation for this study (listed in table 1 in the Appendix).

[6] The images were processed using the CRISM Analysis Tool (CAT) v.7.1 for ENVI following standard procedures [*Murchie et al*., 2007, 2009]. Variations in illumination were corrected to first order by dividing the *I*/*F* image by the cosine of the incidence angle (surface slope derived from MOLA gridded topography at 128 pixels/degree). Atmospheric molecular opacity effects were minimized in the L images by dividing by a scaled atmospheric transmission spectrum over Olympus Mons [*McGuire et al*., 2009]. A denoising algorithm was applied to some of the L images that removes vertical stripes by low-pass filtering in the spatial and spectral domains [*Parente*, 2008]. This denoising algorithm was developed for an older calibration version, but was found to be helpful in some TRR3 images at a less aggressive filtering level. It optimizes the filtering in order to preserve spatial information while correcting systematic noise reintroduced during application of the volcano scan processing. The process then detects and removes spectral spikes by comparing spectral channel values with thresholds and substituting the detected spikes with robust estimates [*Parente*, 2008]. Spectral parameters were calculated for both the S and L images in order to highlight heterogeneity in surface composition [*Pelkey et al*., 2007; *Murchie et al*., 2009]. Spectra were collected for, e.g., 5×5 or 10×10 pixel regions and ratioed to similarly-sized spectrally neutral areas acquired in the same column of the detector in order to cancel instrument artifacts and enhance the spectral features from the surface minerals.

[7] The images were georeferenced and draped over a MOLA terrain model in order to better visualize the relative positions of the phyllosilicate- and carbonate-bearing deposits on the local topography. Three-dimensional (3D) surface views of CRISM data were created using MOLA elevation data for selected images in order to illustrate where the spectra were collected.

[8] A prototype Map-projected Targeted Reduced Data Record (MTRDR) hyperspectral image cube was prepared for CRISM image FRT0000A819. The MTRDR product family [*Seelos et al*., 2012] is a newly defined high-level analysis and visualization data product suite that represents a major advance in the accessibility of CRISM-derived spectral information. The primary MTRDR data product is a full spectral range (VNIR (visible/near-infrared) and IR) spatially coregistered, map projected image cube that has been corrected for atmospheric gas absorptions, normalized to the nearest-nadir sampled geometry to correct atmospheric aerosol scattering and path length effects, normalized to a reference illumination geometry, with bad data bands removed.

2.1.2. CRISM Multispectral Mapping Data

[9] Updated versions of map tiles T0963, T0964, T1035, and T1036 (80°E to 90°E, –2.5°N to 7.5°N) were created as special data products using prototype next-generation software (version 7.1) for normalizing strip to strip variations in aerosol and photometric effects. The original software is described in detail in *McGuire et al*. [2008], and uses historical climatology to predict atmospheric effects for which a first-order correction is performed including variations in surface pressure of CO_2 (from the Viking Lander data) and opacities of dust and ice aerosols and surface and atmospheric temperatures (from TES). The modified software uses data from ongoing missions to predict atmospheric effects including CO_2 using the CRISM Multispectral Mapping (MSP) data itself (based in part on algorithm improvements described in *McGuire et al*. [2009]), and fixed aerosol opacities for dust (0.3) and ice (0.01) contributions. Version 3 of the radiometric calibration was used for the MSP mapping strips in this study. After the MSP mapping strips are corrected for atmospheric, thermal, and photometric effects, they are combined into map tiles for a broader perspective and ease of use [*Malaret et al*., 2008]. Map tiles of the spectral summary parameters are also computed using the algorithms described by *Pelkey et al*. [2007].

2.1.3. CRISM End-member Analyses

[10] The end-member analysis employed here on a recently prepared MTRDR cube for CRISM image FRT0000A819 is based on an automatic end-member extraction procedure [*Parente et al*., 2011]. The algorithm was run on an entire CRISM image for this study. It can also be run on subsections of an image, selected by coordinates, geologic features, or elevated concentrations of minerals of interest obtained from CRISM spectral parameter maps [*Pelkey et al*., 2007].

[11] The algorithm leverages the representation of the hyperspectral image as a "cloud" of spatial pixel vectors (data points) in a space whose number of dimensions equals the number of spectral channels. A nonlinear dimensionality reduction technique enhances the geometric distances between naturally occurring clusters in the cloud that are not immediately evident given the high point density. The technique attempts to capture global nonlinear structures in the data while preserving local differences in the spectral shapes of the image pixels, and to produce well-separated clusters. An unmixing algorithm further analyzes each cluster, which can be

imagined as a spectral "family". This algorithm approximates the roughly convex shapes of the clusters with polyhedra whose vertices are local end-members. The end-members local to all the clusters are collected and screened based on a spectral score, which captures similarity between the spectral shapes of pixels. Two individual pixel spectra are considered similar if their similarity score is larger than a defined threshold.

[12] The reduced set of spectrally unique signatures forms the set of global end-member spectra. Successively, the same similarity score is used to compare the global end-member signatures with spectra from the entire image, and spectral similarity maps for all end-members are created. The threshold for the similarity score is automatically set to ensure that only pixels exhibiting significant similarity to an end-member are included in the similarity map for that end-member. This technique has been validated recently with several CRISM images [*Parente et al*., 2011].

2.1.4. CRISM Tetracorder Analyses

[13] A recently prepared MTRDR cube for CRISM image FRT0000A819 was analyzed using spectral feature shape and position mapping methods described by *Clark et al*. [2003a]. This search process uses spectral features from spectral libraries [*Clark et al*., 2003b, 2007], hypothetical absorptions mathematically constructed using spectral features, and laboratory spectra measured for this study at both Mars-like temperature and terrestrial room temperature to identify and map minerals within the image.

2.2. OMEGA Images and Mineral Maps

[14] OMEGA data were systematically processed according to the standard data reduction schemes (irradiance and atmospheric absorption corrections) that produce reflectance *I*/*F* spectra. Identification and mapping of pyroxene and olivine minerals was performed using spectral parameters [*Poulet et al*., 2007; *Ody et al*., 2012]. Pyroxene is detected by the presence of a broad band centered near 1.9 to 2.3 μm due to Fe^{2+} electronic transitions. An absorption depth threshold of 1% was applied for the pyroxene map. The olivine spectral index measures the slope from 1.0 to 1.7 μm of the right wing of the absorption due to Fe^{2+} in olivine. For global mapping, a threshold of 1.04 was chosen in order to avoid false positives and remove artifacts. This threshold can, however, be adapted for regional studies, and after an extensive manual inspection using ratioed spectra to verify mineral detection and boundaries of olivine-bearing deposits, thresholds between 0.97 and 1.04 have been applied depending on the observational conditions. The spectral parameters were binned into a map of 32 pixels per degree (about 2 km at the equator), which is well adapted to the spatial sampling of OMEGA observations. For pixels observed several times, the highest value of each criterion was used for building maps.

[15] The pyroxene and olivine maps were created using the entire OMEGA data set corresponding to about 3.6 Martian years of observations [*Ody et al*., 2012, 2013]. The data were limited to near nadir-pointing mode (emergence angle $< 15°$, and the images used are listed in Table 1 of the Appendix). High spatial resolution observations with a swath width smaller than 16 pixels were not used because their tracks were too limited (~6 km) to significantly contribute to mapping coverage. In addition, a filtering process was applied to spectra to remove data that include surface frosts, excessive clouds or aerosols, and instrumental artifacts that interfere with OMEGA surface observations as described in detail in *Ody et al*. [2012]. A final data set of 45 data cubes was included in the pyroxene map over this region. For the olivine map, two additional cubes that were previously removed due to the filtering process were added because manual inspections revealed the presence of an olivine signature.

2.3. HRSC Images and Digital Terrain Models

[16] The HRSC instrument onboard Mars Express acquires nearly simultaneous high-resolution, stereo, multicolor, and multiphase angle superimposed image swaths [*Jaumann et al*., 2007]. Four color line sensors and five panchromatic sensors, arranged in different viewing angles and wavelength positions (near infrared: +15.0°; 970 ± 45 nm; green: +2.4°; 530 ± 45 nm; blue: –2.4°; 440 ± 45 nm; red: –15°; 750 ± 45 nm; stereo 1: +18.9°; 675 ± 90 nm; stereo 2: –18.9°; 675 ± 90 nm; photometry 1: +12.8°; 675 ± 90 nm; photometry 2: –12.8°; 675 ± 90 nm and nadir: 0.0°; 675 ± 90 nm), are used to determine photometric surface characteristics and to create digital terrain models (DTMs) [*Neukum et al*., 2004; *Gwinner et al*., 2009]. We utilized radiometrically calibrated and geometrically corrected HRSC nadir image data with a scale of 12.5 m/pixel and corresponding digital terrain models with a scale as good as 50 m/pixel and a vertical accuracy as good as 10 m/pixel [*Scholten et al*., 2005; *Gwinner et al*., 2009]. Further data processing included trimming the images, preparing mosaics, and transforming files in order to incorporate the data into a geographic information systems project using the Environmental Systems Research Institute ArcGIS software. HRSC images used in this study are given in Table 1 of the Appendix.

[17] This software enables superimposing different data sets onto each other and displaying them in a three-dimensional space. Processed HRSC nadir data and DTMs, geometrically corrected CTX image data [*Malin et al*., 2007], and calibrated and projected CRISM parameter maps were incorporated into an ArcScene project in order to visualize the specific locations of different minerals in a geologic context. For the 3D-visualization CTX images were superimposed onto HRSC nadir images. CTX data were only acquired for small-scale diagnostic areas. CRISM visible region (VIS) and IR-RGB composites as well as VIS- and IR-parameter maps were superimposed on the underlying data sets. Each of these images was assigned to the topography provided by an HRSC DTM mosaic of the region. The resulting data set enables visualizing areas of interest from any viewing angle and zoom level providing insight into mineral stratigraphy and geological processes.

2.4. HiRISE Images and DTMs

[18] High Resolution Imaging Science Experiment images are acquired via 14 CCD detectors, each with multiple choices for pixel binning and number of time delay and integration lines [*McEwen et al*., 2010]. Ten CCDs that cover the full swath width (~6 km) are covered by broadband red filters (RED), while four CCDs in the middle are covered by blue-green and near-infrared (IR) filters to provide 3 band color coverage in the center 20% of the image swath. Images are acquired at ~25–30 cm/pixel scale, or ~50–60 cm/pixel in the 2×2 binning mode. Stereo coverage is acquired by imaging a location during two separate orbits, with spacecraft

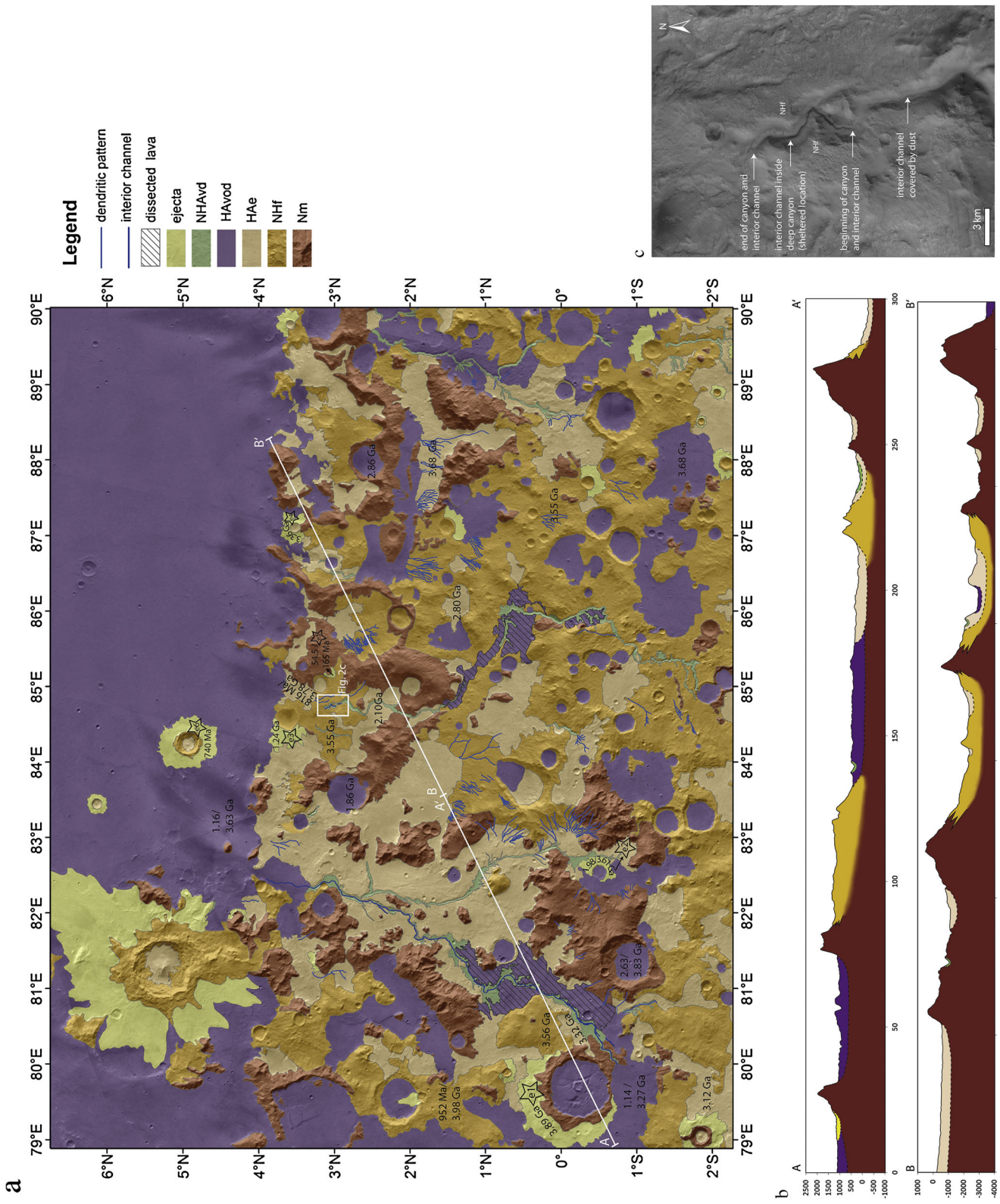

Figure 2. Geology of the Libya Montes region: (a) Regional geologic map with approximate ages as determined in this paper. The geologic units are defined as in recent studies [*Crumpler and Tanaka*, 2003; *Jaumann et al*., 2010; *Erkeling et al*., 2010]. The white line marks the course of the geologic cross-section shown in Figure 2b, the white box indicates the position of Figure 2c. (b) The geologic cross-section from the SE to the NW. The profile has been split into two pieces (*A*-*A*′ and *B*-*B*′) in order to better fit on a page. (c) CTX close-up of the mouth of the middle Libya Montes Valley showing an interior channel winding through a deep canyon. See text for discussion.

rolls that produce stereo convergence angles ranging from 15° to 30°. DTMs are produced by the method described by *Kirk et al*. [2008]. If significant pointing jitter is present, the geometry is first corrected as described in *McEwen et al*. [2010]. Three DTMs have been produced in the Libya Montes region (DTEEC_016034_1835_017089_1835_A01, DTEEC_007727_1830_008808_1830_A01 and DTEEC_002756_1830_002822_1830_A01). These DTMs have a scale of 1 m/pixel and vertical accuracy of ~0.2 m.

[19] Precision overlays of CRISM RGB spectral composites on HiRISE were accomplished by first defining a ground control point network, which is then used as a control network to warp CRISM color composites to the scale of the HiRISE image. The ground control point network is simply defined by colocating identical features in the CRISM IR brightness product (~1.33 μm) and HiRISE and/or CTX grayscale images. A hue-saturation-value transformation was performed [*Gillespie et al*., 1986], using the now warped CRISM color information for hue and saturation, and a HiRISE red mosaic image as a grayscale input for value (i.e., intensity). This procedure merges color information from a CRISM RGB composite (e.g., spectral summary product) with a HiRISE image for precise colocation of spectral units defined from CRISM data with morphologic features in a HiRISE image. The output RGB image has the same pixel scale as the HiRISE red mosaic. This can be taken a step further by overlaying the HiRISE-CRISM composite on a HiRISE-derived DTM (if available) to yield additional stratigraphic and geometric context in 3D.

2.5. Geologic Maps and Chronology

[20] Digital geologic mapping was performed using HRSC image and terrain data with ArcGIS. We worked with a mapping scale of 1:200,000 in order to combine adequate detail with sufficient context information to identify the features. For the final map presentation we used a Viking background map because the spatial resolution (231 m/pixel) of this regional data set better fits the visualization scale of 1:2,000,000.

[21] The nomenclature of our mapping units largely follows the convention established by *Crumpler and Tanaka* [2003] and *Jaumann et al*. [2010]. Because we used a higher resolution data set for the geologic mapping in this study, this new map likely represents a refinement of the earlier work and may include some subtle differences. We have also combined some of the mapping units and introduced new normalized units because this generalization better meets the scientific objectives of this paper to illustrate general trends for the region.

[22] Crater retention age dating was performed by means of the crater size-frequency distribution of a defined geologic surface fitted to a model crater production function [*Hartmann and Neukum*, 2001; *Neukum*, 1983; *Neukum and Hiller*, 1981]. The frequency of specific crater sizes together with a calibrating chronology function are used to estimate the absolute surface ages of the landscape [*Michael and Neukum*, 2010]. This provides a minimum age or resurfacing age for the geologic units. We used the chronology function of *Hartmann and Neukum* [2001] and the production function of *Ivanov* [2001]. Crater counting was also performed using HRSC data, employing an ArcGIS tool for the mapping and extraction of craters, developed and described by *Kneissl et al*., [2011], plus a software tool called "craterstats" [*Michael and Neukum*, 2010] for visualization of the plots of the crater density analysis. In general, secondary clusters are excluded where visibly identifiable. The spatial randomness analysis (see section 3.1.7) is used to confirm that the crater population is not clustered. The minimum crater diameter used for crater counting was 150 m.

3. Characteristics of the Libya Montes Region

[23] The geology and mineralogy of the Libya Montes region were studied here through coordinated analyses of multiple data sets. Geologic and mineralogic context for the region were assessed through analyses of images collected by OMEGA, CRISM (multispectral survey mode), HRSC, and CTX. Stereo HRSC views and crater counting enabled age constraints on the geologic units. HiRISE and high-resolution targeted CRISM images were used for detailed study of the morphology and composition of specific sites.

3.1. Geology

[24] The new geologic map of the Libya Montes region (Figure 2a) covers about 79°E to 90°E and 2°S to 6°N, including the western, middle and eastern valleys as named by *Crumpler and Tanaka* [2003], several fluvial features, and numerous impacts. A geologic cross-section was also constructed from the southeast to the northwest of the study region (Figure 2b). The route of the cross-section (*A-A′* / *B-B′*) is indicated by a white line in Figure 2a. The geologic units are introduced separately and summarized in Table 1.

Table 1. Geologic Units Present in Figures 2 and 3

Symbol	Name	Description
Nm	Noachian massif -old Noachian bedrock, remnants of Isidis impact crater rim	(3.9 to 3.7 Ga)
NHf	Noachian/Hesperian fluted and dissected terrain -fluvial dissected bedrock	(3.98 to 3.45 Ga)
HAe	Hesperian/Amazonian eroded material -heavily degraded material, fluvial and aeolian erosion, partial remnants of lava flows	(3.78 Ga to 816 Ma)
HAvod	Hesperian/Amazonian volcanic deposits	(3.83–1.14 Ga)
HAvod	Hesperian/Amazonian volcanic deposits	(3.83–1.14 Ga)
NHAvd	Noachian/Hesperian/Amazonian valley deposits (no absolute ages) -valley deposits along the course of broad fluvial valleys, fluvial and lava deposits	
Ejecta	ejecta blanket of impact craters	(3.89 Ga to 54.5 Ma)

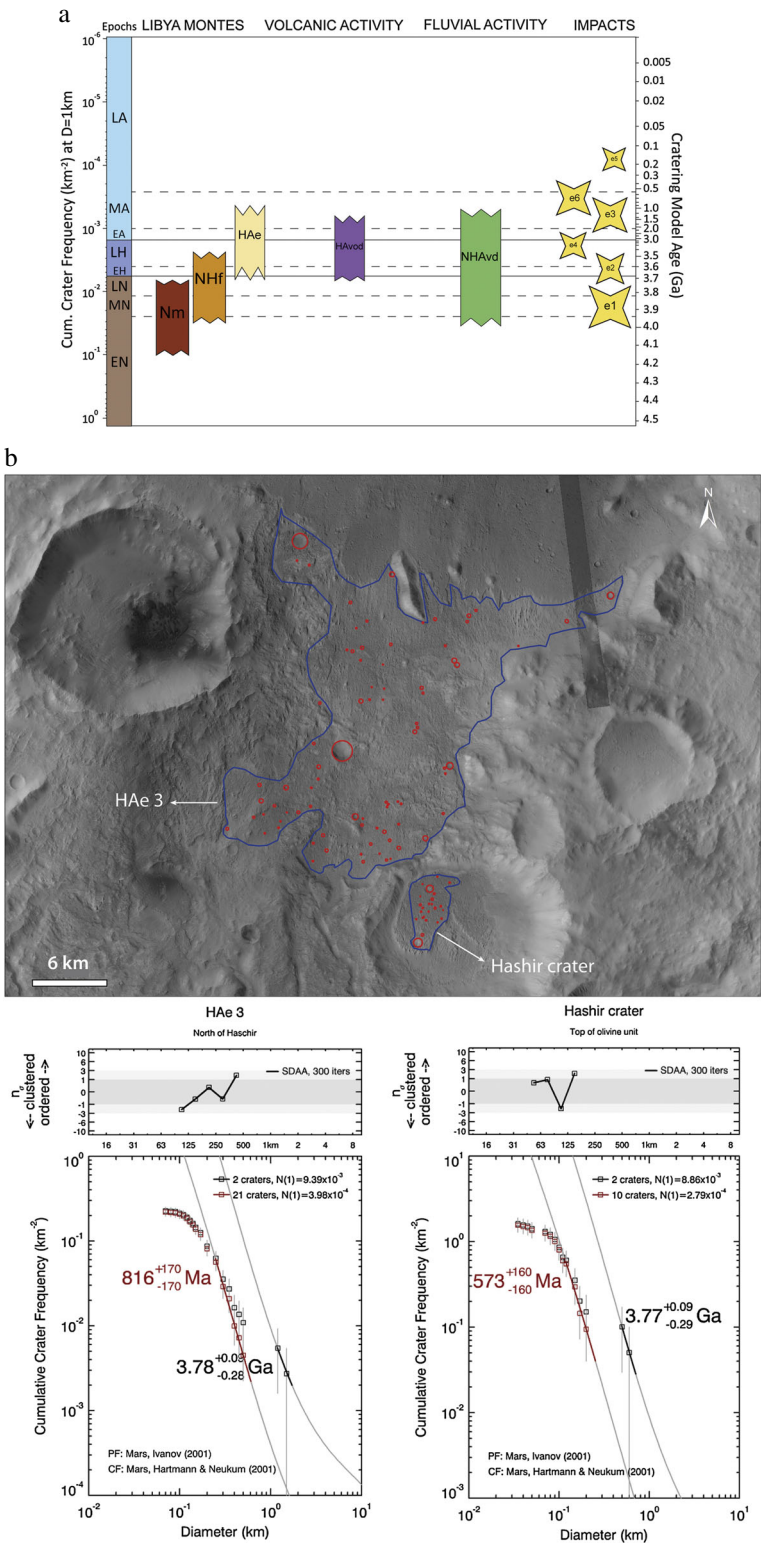

Figure 3. Model ages for terrain in Libya Montes based on a size-frequency distribution of retained crater counting: (a) Cratering modeled ages determined for volcanic, fluvial and impact sites in the region, and (b) crater size-frequency measurements for the post-impact fill materials within Hashir Crater (both olivine-poor and olivine-rich) and a region north of Hashir Crater containing olivine- and phyllosilicate-bearing outcrops. Outlines of the crater counting areas are shown in blue, counted craters are shown in red. Cratering modeled age diagrams show the initial surface age and the resurfacing age for the counted areas. Above the crater count plots are diagrams showing the results of the randomness analyses. According to these diagrams both crater populations are neither clustered nor ordered and are thus suitable for age determinations making the results more reliable. See text for detailed explanation.

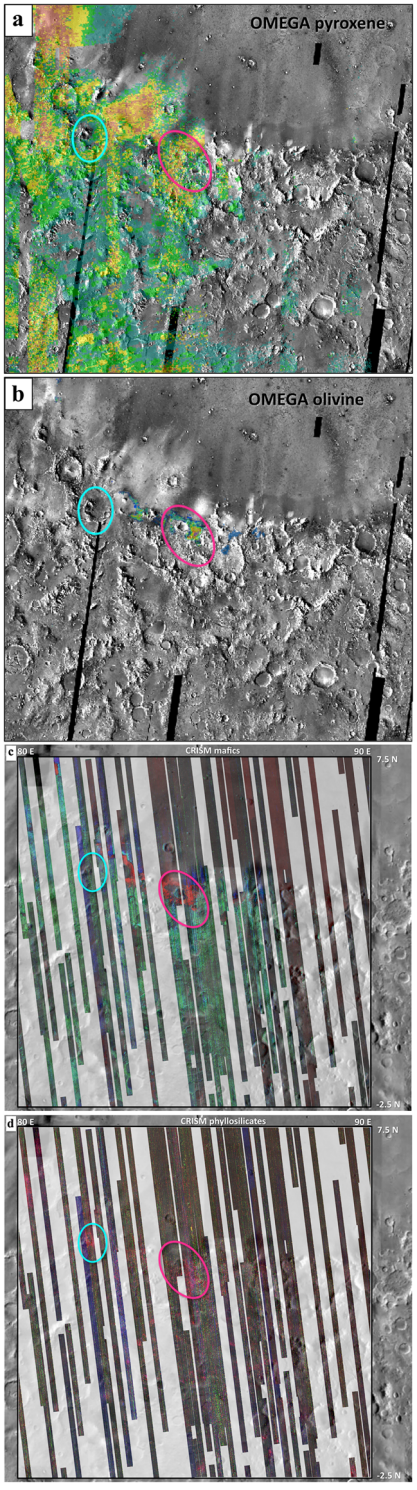

Figure 4. Regional mineralogy maps for Libya Montes: (a) olivine from OMEGA using a spectral parameter based on the olivine absorption band near 1 µm (OSP2 in *Ody et al*. [2012]); (b) pyroxene from OMEGA using a spectral parameter based on the ~2 µm pyroxene absorption band [*Poulet et al*., 2007; *Ody et al*., 2012]; (c) CRISM maptiles T1035, T1036, T0963 and T0964 with R OLV, G LCP, B HCP; and (d) same CRISM maptiles with R d2300, G bd2210, B bd1900. Blue and pink ovals mark regions of detailed studies.

3.1.1. Noachian Massif Unit

[25] The oldest units mapped in the study region are ancient highland basements characterized by rugged mountainous relief labeled Noachian massif (Nm). They can occur as individual peaks or massif chains with steep slopes and sharp crests reaching the highest elevations in the Libya Montes area. These mountainous massifs were likely uplifted in the Early Noachian, at the time and as a consequence of the formation of the Isidis Basin around 3.96 Ga [*Werner*, 2005, 2008]. As such, the rocks of this unit are composed of ancient crust formed prior to the Isidis event based on their occurrence within the modified rim-terrace complex of the impact basin. The youngest of these Nm units have a model age of 3.7 Ga and predate the fluted and dissected terrains labeled as NHf (Noachian/Hesperian fluted).

3.1.2. Noachian/Hesperian Fluted and Dissected Terrain Unit

[26] These intensely degraded highland materials date from 3.98 to 3.45 Ga and predominately consist of fluvially dissected surfaces of medium elevation. Portions of this unit could have been originally derived from Isidis ejecta, although this cannot be identified as a distinct unit due to heavy modification of the terrain. The valleys incised into this unit are narrow, parallel in pattern, and highly degraded.

3.1.3. Hesperian/Amazonian Eroded (HAe) Unit

[27] The Hesperian/Amazonian eroded material presents a unification of Hesperian to Amazonian aged surfaces (3.78 Ga to 816 Ma) featuring different erosional patters. It comprises the units Hi (intermountain plains) and Hd (dissected plains) as mapped by *Crumpler and Tanaka* [2003]. The map in Figure 2 covers a broader area than recent studies [*Erkeling et al*., 2010; *Jaumann et al*., 2010; *Crumpler*, 2012] in order to provide an overview of the geology across a regional mapping scale. The HAe (Hesperian/Amazonian eroded) unit lies topographically above the NHf and Nm units but can occur at the same elevation as the Hesperian/Amazonian volcanic deposit (HAvod, described below) and is predominantly flatter than NHf. Parts of the HAe unit might have formerly been smooth basaltic lava flows, as indicated by flow fronts along many geological contacts, but are now highly degraded, modified, or even redeposited, so that we consider this differentiation to be reasonable. The rough (on the meter scale) and etched HAe surface has been shaped by fluvial and aeolian erosion and often features yardangs, groves, and small channels.

3.1.4. Hesperian/Amazonian Volcanic Deposit Unit

[28] The Hesperian/Amazonian volcanic deposits include lava flows and ash deposits of different ages, presumably originating from the volcanic province Syrtis Major to the west. They were primarily identified by flow fronts along the geological contacts. Extensive lava surfaces also cover the Isidis Basin and the floors of many filled impact craters. We discriminate between smooth (on the meter scale) lava surfaces, which are only blotched by small craters and interrupted by wrinkle ridges, and distinctly dissected lava. The latter can be identified by the hatching symbols in the geologic map of Figure 2a. This unit appears to be mainly eroded by fluvial processes and preferably traced along the course of the fluvial valley systems (see Figure 2a), but is still smoother overall (on the meter scale) than HAe. Crater counting on the volcanic deposits yield ages from Early Hesperian to Middle

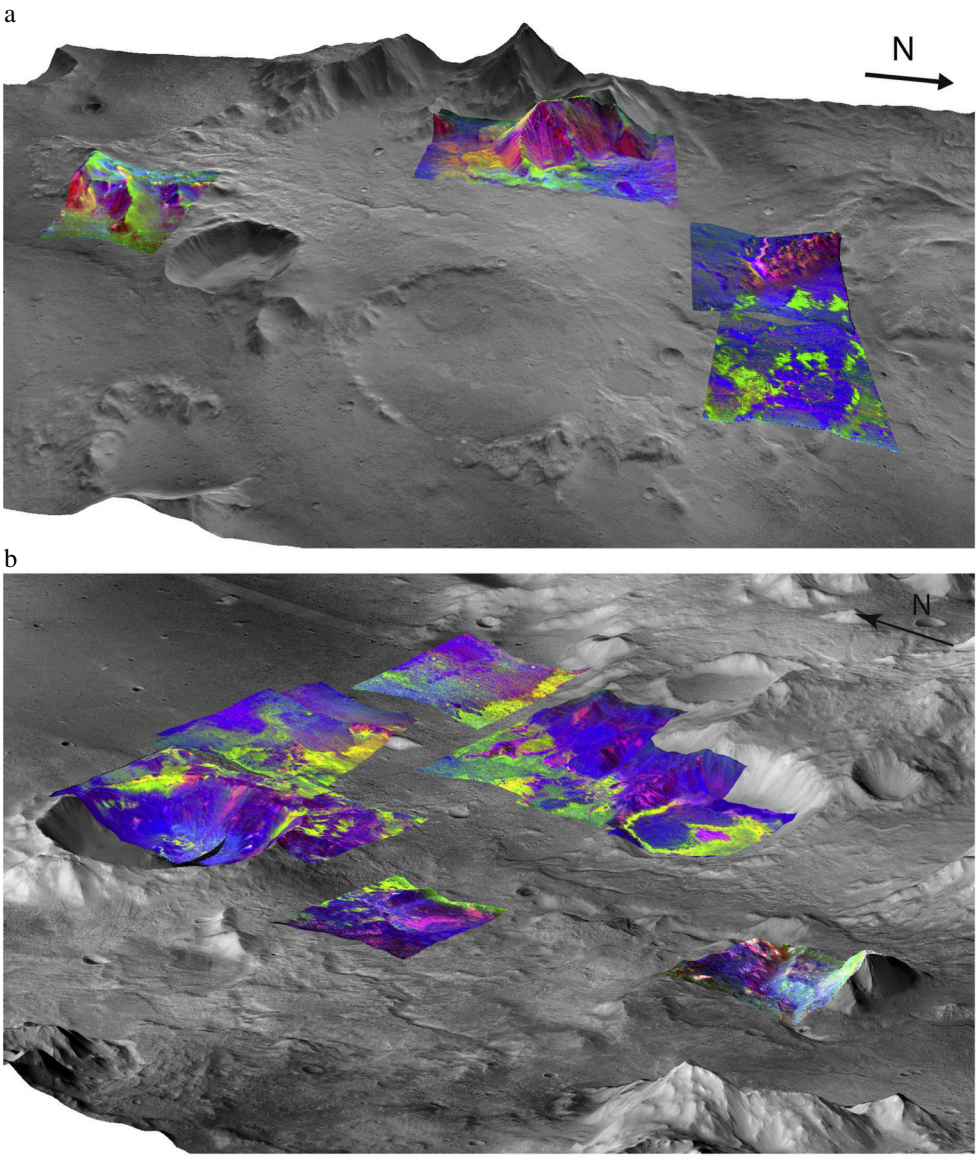

Figure 5. CRISM mineral maps prepared with R D2300, G OLINDEX, B LCP parameters over HRSC DTMs overlain onto CTX imagery: (a) western region where mafic minerals and aqueous outcrops are exposed on the surface, and (b) central region where mafic minerals and aqueous outcrops are exposed on the surface. Fe/Mg-smectite is shown in pink, olivine in green-yellow, and pyroxene in blue.

Amazonian times (3.83–1.14 Ga), which is consistent with the findings of previous studies [e.g., *Jaumann et al*., 2010; *Skok et al*., 2010; *Tanaka et al*., 1992] and mirrors multiple phases of volcanic overprint in the Libya Montes region.

3.1.5. Noachian/Hesperian/Amazonian Valley Deposits Unit

[29] The ages of the terrains with valley network deposits range from Noachian to Amazonian [*Jaumann et al*., 2010], as revealed by dating of fluvially incised lava flow surfaces as well as HAe and NHf surfaces. These Libya Montes valley networks drain northward downslope toward Isidis Planitia over a distance of more than 300 to 400 km (from the western and central Libya Montes regions, respectively). Fluvial channels forming as dendritic patterns are incised into older NHf and Nm units. These oldest parts of the valley deposits date almost exclusively to ancient terrain of the Noachian and Early Hesperian periods. The regional geologic context indicates that these channels represent remnants of former complex dendritic fluvial systems draining into the longitudinal main channels [cf. *Jaumann et al*., 2010, Figure 3a]. In other places, the former course of the dendritic systems cannot be reconstructed because erosion and infill of HAvod and HAe material obscures the proposed previous channel passages. An interior channel (i.e., a narrow channel inside of a broader fluvial valley representing the actual river bed) can only be traced along the western Libya Montes Valley, and characterizes the course of the ancient river bed that was carved through

repeated fluvial activity [*Irwin et al*., 2005; *Jaumann et al*., 2005]. The central Libya Montes Valley does not feature many of these narrow channels likely because prolonged dry conditions as well as aeolian and volcanic infilling have eroded and smoothed out this region. However, there is one place where a channel cuts through the old NHf unit at the very northern part of the central Libya Montes Valley (Figure 2c). Because the channel is obscured right before and after this valley section, we deduced that this channel does not indicate a late, locally restricted fluvial activity, but was protected from infilling through its sheltered geographic location (Figure 2c). Based on our crater counting of the terrains incised by the channels the latest fluvial activity of this middle valley network dates back to the Noachian/Hesperian boundary about 3.74 Ga.

3.1.6. Ejecta Units

[30] Several impact craters in the study region have fairly well preserved ejecta blankets. Dating of a selection of these

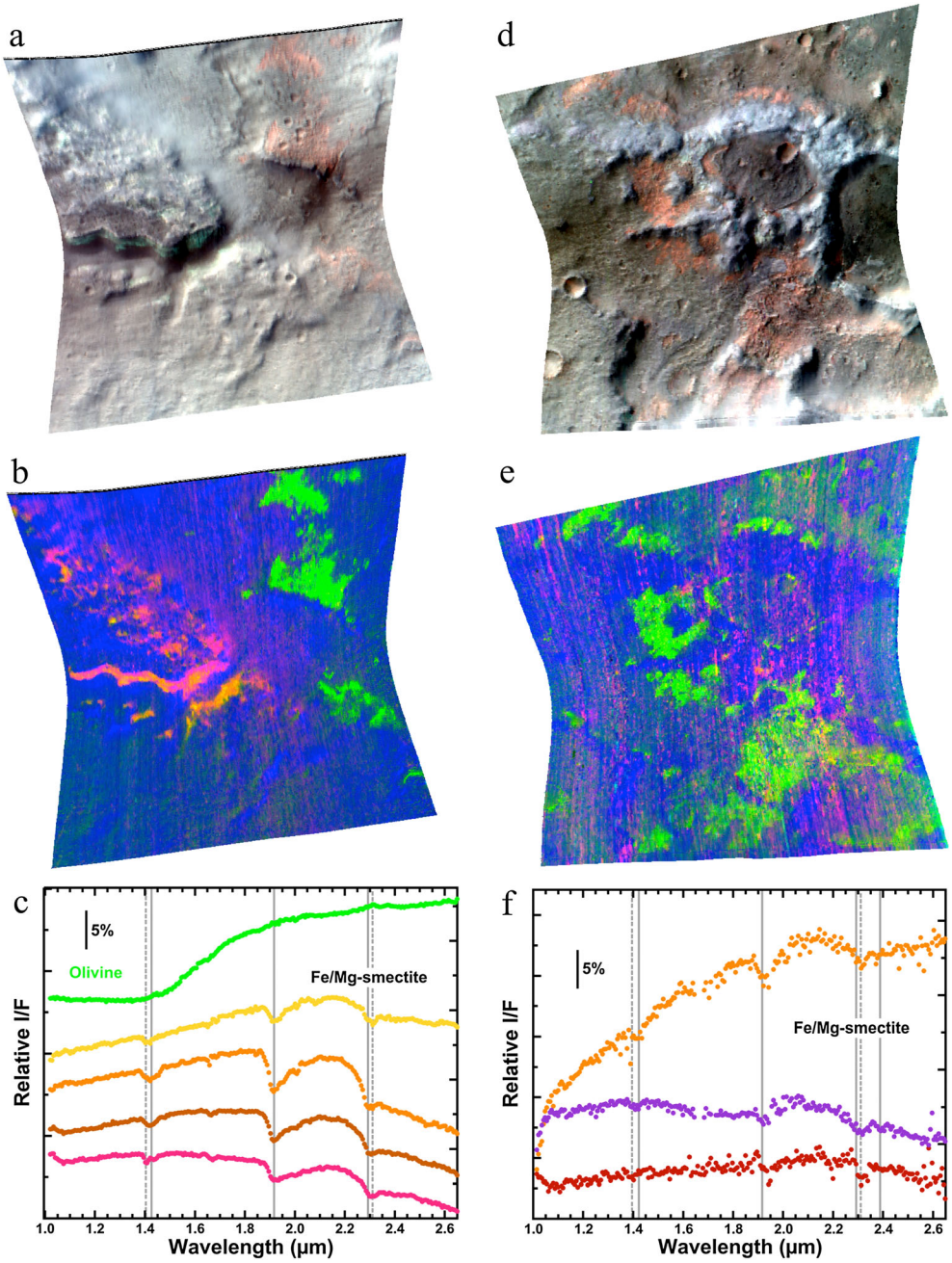

Figure 6. CRISM images FRT0000A909 and FRT00023777 of the western phyllosilicate outcrop: (a) FRT0000A909 prepared with R 2500 nm, G 1500 nm, B 1208 nm; (b) FRT0000A909 prepared with R D2300, G OLINDEX, B LCP parameters; (c) ratioed *I*/*F* spectra 1.04–2.65 μm from FRT0000A909 with a 5% band depth scale bar; (d) FRT00023777 prepared with R 2500 nm, G 1500 nm, B 1208 nm; (e) FRT00023777 prepared with R D2300, G OLINDEX, B LCP parameters; (f) ratioed *I*/*F* spectra 1.04–2.65 μm from FRT00023777 with a 5% band depth scale bar.

yielded ages ranging from 3.89 Ga to 54.5 Ma years. The oldest dated crater (e 1, Figure 2a, Appendix A) is the 47 km diameter crater at the source region of the Western Valley System. We find that the crater floor is filled with fractured lava units, which seem to be directly attributed to volcanic processes within the crater [*Jaumann et al*., 2010; *Bamberg et al*., 2012]. The youngest dated ejecta blanket (e 5, Figure 2a, Appendix A) was exposed by the ~5 km diameter crater located at the southeast of the rim of Hashir Crater. It is possible that parts of this ejecta blanket were deposited inside Hashir Crater and are represented by the landslide-like depositions at Hashir's eastern crater wall. The chronological relationships of the mapped geologic units are displayed in Figure 3a. The crater count plots for all dated surfaces are listed in Appendix A.

3.1.7. Crater Counts

[31] An example crater counting model is shown in Figure 3b for the central Libya Montes region. The rest of the data are given in Appendix A. The results for each site include an outline of the dated areas and the counted craters as well as the resulting crater count plots. The latter features a diagram of the randomness analysis, an automated quality assessment technique that measures the degree of clustering of the counted craters. Clustering could indicate either that the mapped area is not homogeneous in its geologic history or that secondary craters were counted, making the count unsuitable for dating. This quantitative procedure is implemented into the software "craterstats" and was described in detail by *Michael et al.* [2012]. It bins the counted craters into groups of certain size ranges and tests statistically how these craters would be arranged on the surface if they were distributed randomly. The results are compared with the actual distribution of the counted craters and the degree of clustering is calculated and shown in the diagram. Acceptable values range inside the grey to light-grey zones of the diagram (neither clustered nor ordered). Hence, it gives a general view of the quality of the counting as long as the graph in the diagram is located inside this zone. We used the Standard Deviation of Adjacent Area method for all of our crater counting because it was found to be the most sensitive measure for our study [*Michael et al*., 2012].

[32] Both crater count plots show two model ages, indicating that the dated surfaces have experiences resurfacing events. The older ages 3.77 Ga and 3.78 Ga display the original age of the underlying units as represented by the larger craters on the counted surfaces. The resurfacing event was the deposition of the olivine-rich caprock material after the formation of Hashir Crater resulting in covering smaller

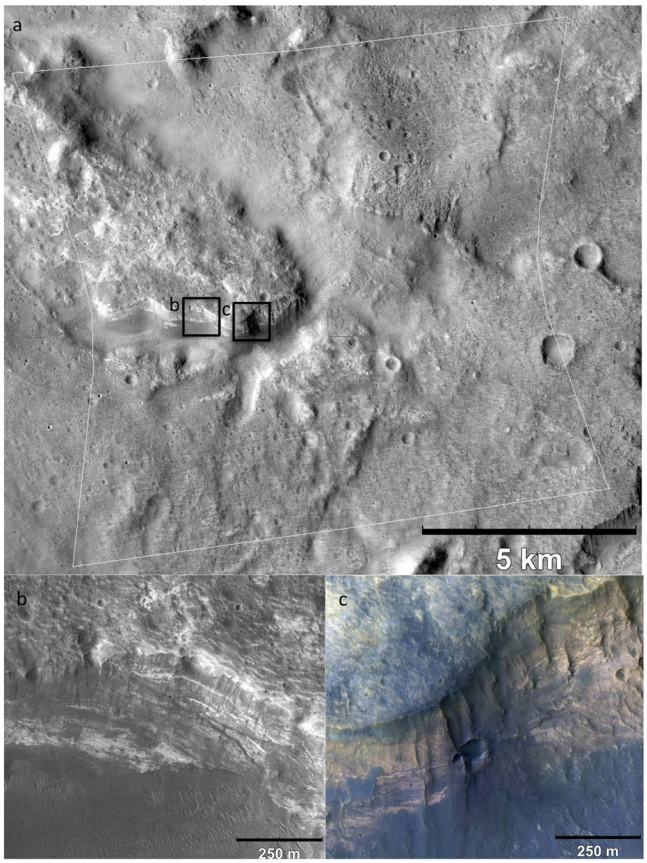

Figure 7. Morphology of Fe/Mg-smectite-bearing unit from CTX and HiRISE. (a) CTX image P04_002466_1843 of the region shown in Figure 6. (b) Close-up of an outcrop with a characteristic light-toned appearance and what appears to be layering in HiRISE image ESP_027559_1845. (c) Close-up of a region just to the east of Figure 7b where there is color HiRISE coverage that shows distinctive IRB colors of orange and yellows that correlate with the Fe/Mg-smectite-bearing unit.

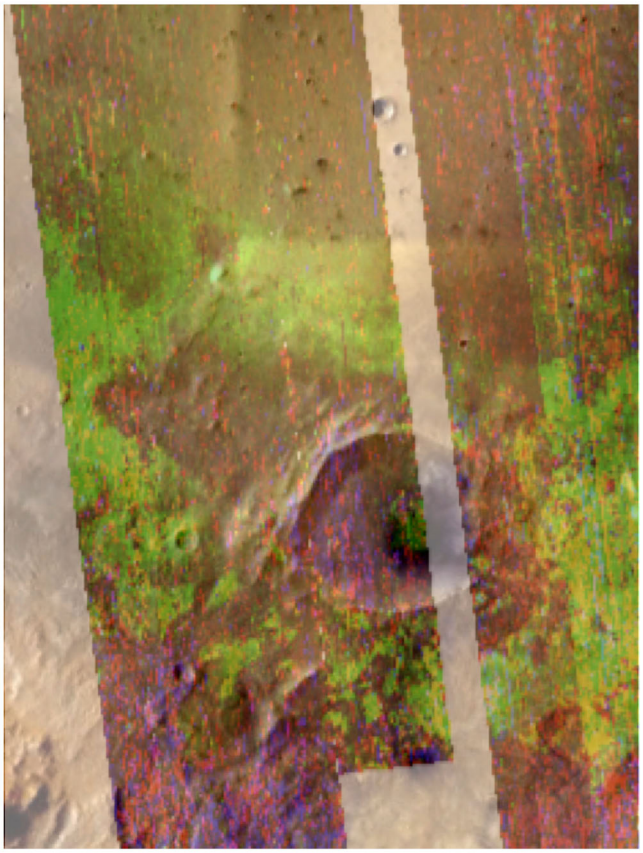

Figure 8. CRISM map tile #T1035 over HRSC for region surrounding Duvolo Crater showing a portion of the central Libya Montes mafic and phyllosilicate outcrops prepared with R D2300, G OLINDEX, B LCP parameters.

craters on the original surface, and thus, cutting the cratering curve. Subsequent cratering on top of the olivine-rich units results in the younger resurfacing ages of 574 Ma and 816 Ma years. Grooves and yardangs evidence intense aeolian erosion of these olivine-rich units, probably eroding some of these subsequent craters. Hence, it could be reasonable that the olivine units are slightly older than indicated by these resurfacing model ages.

3.2. Mineralogy and Morphology of Geologic Units

[33] Pyroxene is well correlated with low albedo and relatively dust-free regions located both in the Libya Montes rim and in the Isidis Basin in the western part of our study region (Figure 4). *Tornabene et al*. [2008] identified three distinct forms of pyroxene-bearing units in this region: pyroxene-rich massifs, pyroxene-bearing caprock and windstreaks associated with a pyroxene signature. Pyroxene-bearing caprock is observed in some more recent, possibly Amazonian units while ancient pyroxene-bearing basalts are also found in Noachian regions [*Tanaka et al*., 1992]. In the highlands, the pyroxene-bearing caprock tends to embay the higher-standing mountain features. The surface morphology of the pyroxene-bearing caprock unit has a smooth texture disturbed by the presence of small-sized craters (<1 km) in THEMIS visible images. Although it is often observed as discontinuous discrete patches, the morphologic similarities between these various occurrences suggest that they are of a similar origin and that they were emplaced as a flow. Given their close proximity to Syrtis Major, we propose that these deposits are lava flows emanating from Syrtis Major that infiltrated the basin and some part of the highlands from the west and southwest consistent with previous studies [e.g., *Tornabene et al*., 2008].

[34] The olivine-bearing terrains are found in the transition boundary between the Libya Montes Noachian crust and the Isidis basin floor (Figures 4b and 4c). The OMEGA-based spatial distribution of olivine [*Ody et al*., 2012, 2013] is in excellent agreement with mapping based on TES and THEMIS data [*Tornabene et al*., 2008]. The higher abundance of olivine near Isidis basin has been invoked to ascribe the origin of the olivine-rich unit to Isidis impact melt [*Mustard et al*., 2009]. The stratigraphy of the units may also provide some information about origin of the units. In some locations, both CTX and HiRISE images clearly reveal that the pyroxene-bearing caprock conformably overlies the olivine-rich materials, consistent with observations from THEMIS visible images and Mars Orbiter Camera [see *Tornabene et al*., 2008]. Clues about the regional stratigraphy were provided by the THEMIS detection of olivine associated with impact craters that occur on the Isidis plains, which demonstrated that an olivine-rich unit lies beneath the plains of Isidis at least 90 km from the transition boundary [*Tornabene et al*., 2008]. An olivine-bearing unit has been observed in some regions of Syrtis Major as well, although the position of this unit in relation to the pyroxene-rich lavas is uncertain due to the low abundance of this olivine-bearing unit [*Pinet et al*., 2007]. Thus, an Isidis impact melt origin for the olivine-rich unit is supported by the proximity of the primary outcrops of this unit to Isidis, while the Syrtis lava flow origin for this unit is supported by the stratigraphy of pyroxene-bearing caprock covering an olivine-rich unit in the vicinity of Syrtis Major's eastern extent, which includes the Isidis plains.

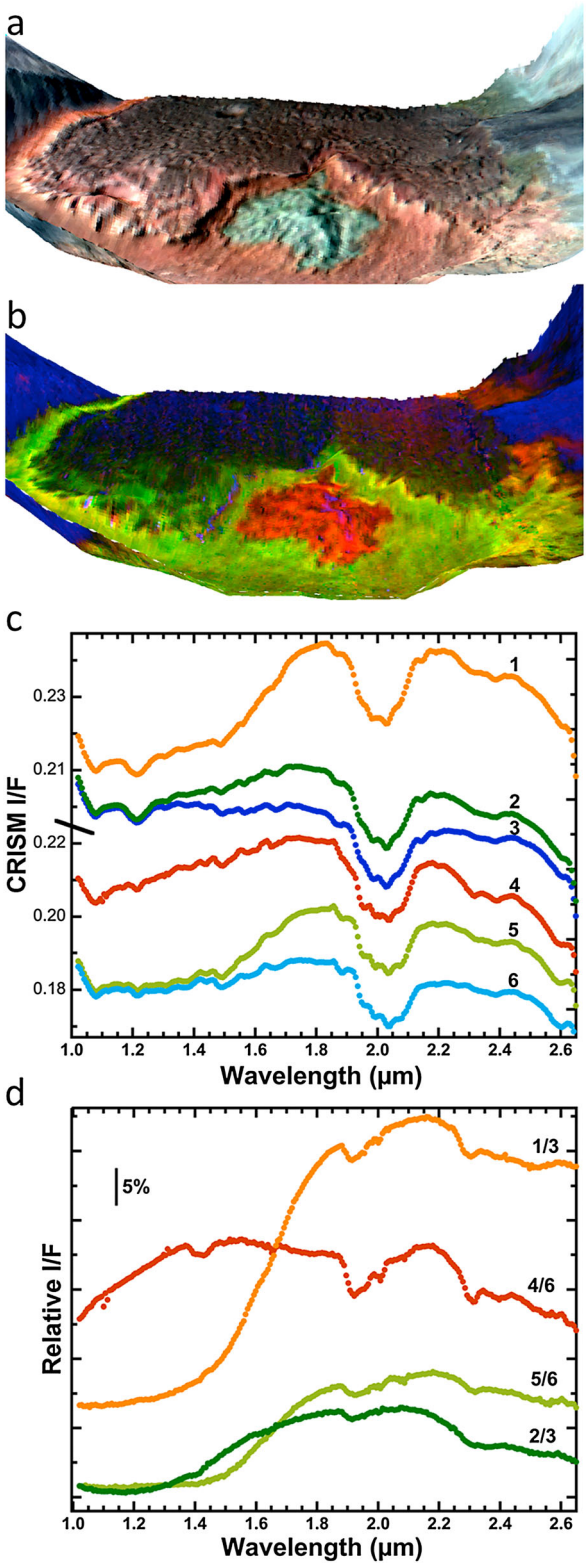

Figure 9. (a) 3D view of CRISM image FRT00047D8 of Hashir Crater prepared with R 2529 nm, G 1506 nm, B 1080 nm, 10× vertical enhancement. (b) 3D view of CRISM image FRT00047D8 of Hashir Crater prepared with R D2300, G OLINDEX, B LCP parameters, 10× vertical enhancement. (c) CRISM *I*/*F* spectra 1.04–2.65 μm. (d) Ratioed CRISM *I*/*F* spectra 1.04–2.65 μm with a 5% band depth scale bar.

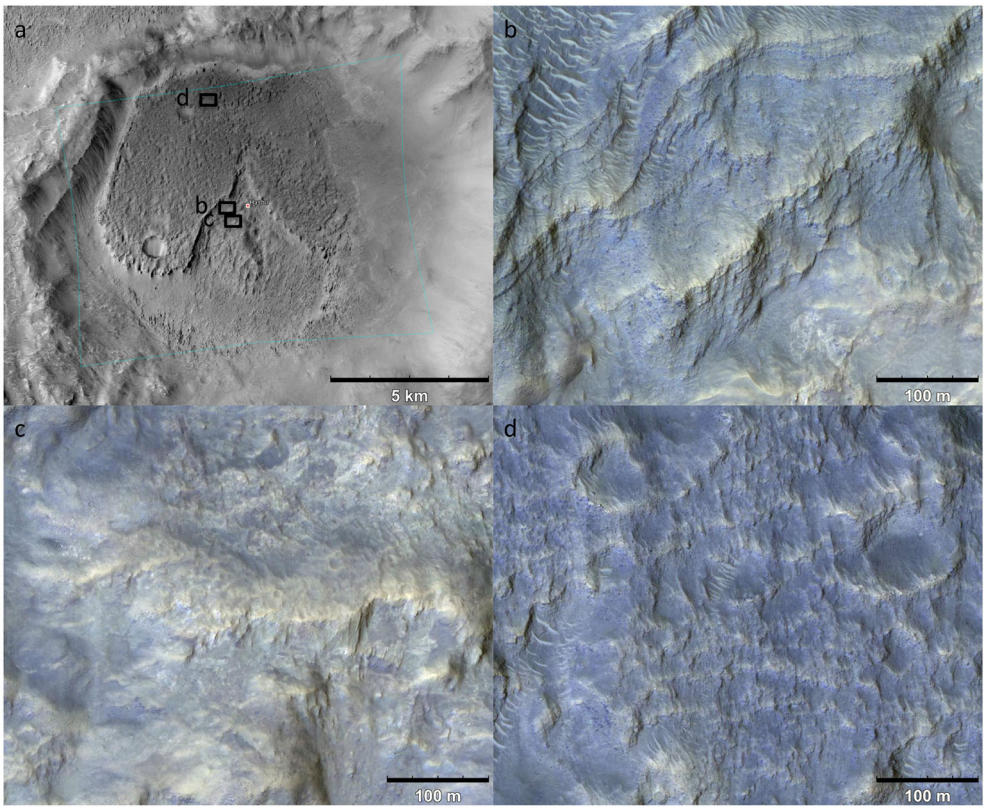

Figure 10. Morphology of Hashir Crater site. (a) CTX image P05_016034_1834 of Hashir Crater with outline of CRISM image FRT000047D8 marked in blue, (b) expanded view of olivine-rich unit from HiRISE image PSP_002822_1830_IRB, (c) expanded view of Fe/Mg-smectite-rich unit, and (d) expanded view of crater interior including some aeolian material and/or eroded caprock covering the olivine-rich surface.

[35] Detailed mineralogical analyses in this study are focused on observations in two regions of Libya Montes indicated by ovals in Figure 4. A region in western Libya Montes near 4°N and 82°E exhibits abundant mafic outcrops and some Fe/Mg-phyllosilicate exposures (Figure 5a). A region of central Libya Montes near 3°N and 85°E exhibits abundant Fe/Mg-smectites, olivine and pyroxene in several CRISM images (Figure 5b). Spectral parameters were used to map these mineral components [e.g., *Pelkey et al*., 2007] and the low-Ca pyroxene parameter worked best to highlight the pyroxene component, although the spectra are consistent with the presence of both high-Ca and low-Ca pyroxene in the basalt. Some of these materials correlate with outcropping bedrock, ejecta from impacts, and deposits formed from aeolian and fluvial activity. Multiple fluvial features are also observed here. Additional views of these images are available in the Supporting Information.

3.2.1. Western Libya Montes Region

[36] Mineralogy of the western Libya Montes region is illustrated through analyses of two targeted CRISM images shown in Figure 6. Spectral features characteristic of olivine and pyroxene are observed here as well as small regions along the walls of a channel that exhibit spectral features due to phyllosilicates (Figures 6b and 6c). Olivine-bearing basalt is identified by a single, broad Fe^{2+} electronic absorption near 1–1.4 μm in the CRISM spectra, while pyroxene-bearing basalt contains weaker Fe^{2+} electronic absorptions near 1 and 2 μm [e.g., *Burns*, 1993]. The bands near 1.43, 1.91, 2.29, and 2.39 μm are consistent with Fe/Mg-smectite and small shifts in these features are consistent with variations in the relative abundance of Fe and Mg in the smectite structure. The phyllosilicate-bearing units may be more extensive than seen here as they could be covered by dust and sand. One occurrence of the Fe/Mg-smectite features within a cliff-forming lobate deposit in this region is particularly intriguing (Figures 6a, 6b, and 7). Based on detailed mapping (Figure 2) and context images the deposit is consistent with a portion of the layered ejecta deposits originating from Beruri Crater. Views from CTX and HiRISE (Figure 7) show the detailed morphology of this Fe/Mg-smectite-bearing unit. There are bright layers in the smectite-rich units, which are likely in situ concentrations of altered materials within the Beruri layered ejecta. In some locations (Figure 7b) the smectite-rich units in the Beruri ejecta correspond to crudely layered materials, while in the HiRISE color views they are consistent with the Fe/Mg-smectite-bearing unit in the Nili Fossae region [*Delamere et al*., 2010]. The olivine-rich bedrock in this region has distinctive polygonal or jointed textures at the meter scale and is a cliff-forming unit (resistant to erosion) that often appears strongly layered. The pyroxene-rich unit is also resistant but is heavily cratered and appears mantled, perhaps by impact-generated regolith. Stratigraphically, the pyroxene-rich unit overlies the olivine-rich unit in Figures 6–7. The smectite-rich unit clearly underlies

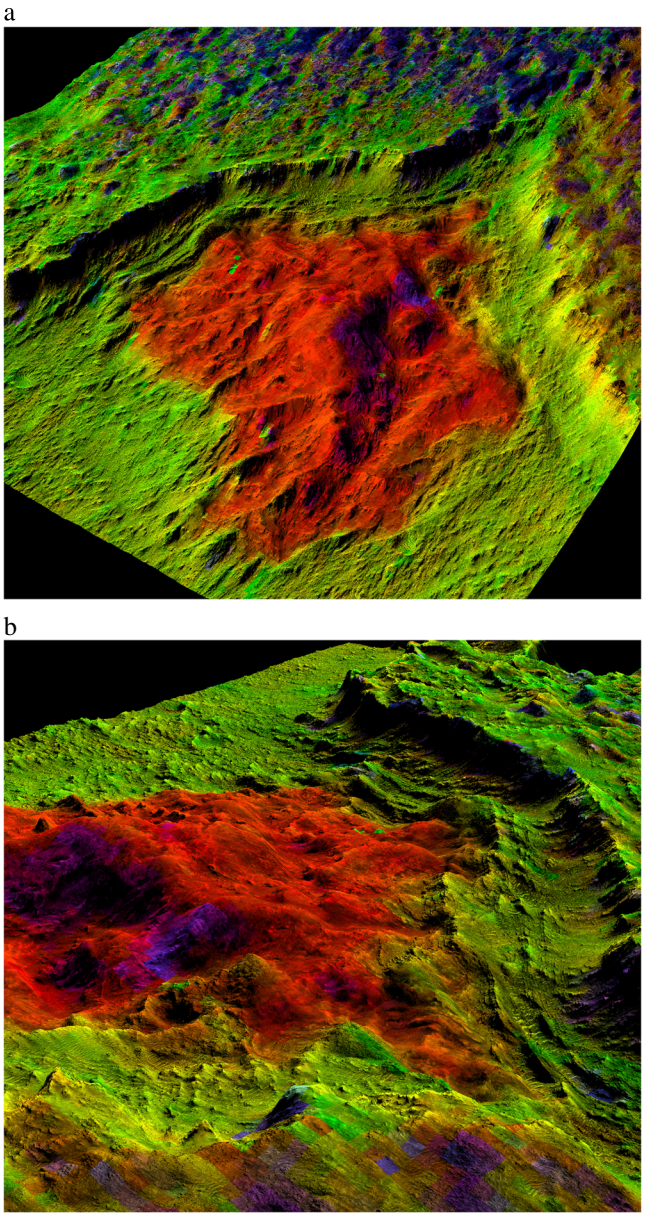

Figure 11. 3D perspective images of Hashir Crater generated by combining a CRISM spectral summary parameter color image with an orthorectified HiRISE red mosaic image (DT1EA_002756_1830_002822_1830_A01), which is draped over a HiRISE stereo-derived DTM (DTEEC_002756_1830_002822_1830_A01) with a 3× vertical \enhancement: (a) view from southeast illustrating pyroxene-bearing caprock in blue on top of olivine-bearing layered bedrock in green, which in turn overlies an Fe/Mg-smectite bearing unit in red, and (b) another view from the east that illustrates the layering and eroding of the olivine-bearing unit and how it embays and superposes the Fe/Mg-smectite-bearing unit, which is interpreted to occur within the central uplift of Hashir Crater (see text). Scale varies due to the 3D geometry, but the width of the composite is ~5.4 km.

the pyroxene-rich unit in Figure 7. The occurrence of the smectite-rich unit within the Beruri layered ejecta suggests that the smectite-rich unit lies stratigraphically below the olivine-rich unit. The smectite-rich unit was likely excavated from beneath the olivine-rich unit based on its occurrence in the Beruri ejecta, however this does not preclude the idea that these clays may have been formed through impact-induced mechanisms related to the formation of Beruri Crater.

3.2.2. Central Libya Montes Region

[37] The mineralogy of the central Libya Montes region includes olivine and pyroxene-rich rocks and more abundant phyllosilicate outcrops than observed in the western region. A mineralogy map produced from the CRISM multispectral images highlights Duvolo Crater (Figure 8) and shows olivine deposits that dominate the western portion of the crater and the presence of Fe/Mg-phyllosilicates east of the crater. Pyroxene-bearing units are also observed here. Several targeted CRISM images from this region are analyzed in more detail to describe the kinds of aqueous minerals present. Each of these is accompanied by a set of HiRISE views to determine their detailed morphology.

[38] Hashir Crater is located southeast of Duvolo Crater at 84.56°E, 3.63°N and illustrates well the stratigraphy of the Fe/Mg-smectite, olivine, and pyroxene units characteristic of the Libya Montes region. Mineralogic maps and spectra from CRISM image HRS000047D8 are shown in Figure 9 for Hashir Crater. Examples of the olivine and phyllosilicate unit morphologies are shown in Figure 10.

[39] Views from the HiRISE DTM colored using CRISM mineralogy are shown in Figure 11. The Fe/Mg-smectite-bearing unit (red) is seen here exposed in the central uplift of Hashir Crater, which is overlain and embayed by layered olivine-bearing rocks (green) overlain by pyroxene-bearing caprock (blue). We interpret the stratigraphy with the olivine-rich unit overlying the smectite-rich unit. Based on these stratigraphic relationships, and the local geologic setting (Hashir Crater), the layered olivine-bearing rocks must postdate the Hashir forming impact-event.

[40] Targeted CRISM image FRT00018800 is located west of Hashir Crater and also displays views of the olivine-bearing lava covering the ancient Fe/Mg-smectite-bearing unit. Fe/Mg-smectite is abundant in this image and occurs mixed with olivine in some locations and mixed with both olivine and another material (likely carbonate, chlorite, or serpentine) in at least two smaller locations. 3D mineralogy maps and spectra are shown in Figure 12, and the morphology of selected units is shown in Figure 13. The olivine-bearing unit exhibits polygonal cracking and a blocky texture and appears to be covered by aeolian ridges in some places (Figure 13b). The 300 m wide bright-toned Fe/Mg-smectite-bearing patch in Figure 13c exhibits layering and appears to be partially covered by the olivine-bearing unit to the south. A view of the largest Fe/Mg-smectite outcrop is shown in Figure 13d. This unit is ~3 km across and exhibits polygonal cracking similar to the olivine-bearing unit, but the surface appears more altered and eroded.

[41] Approximately 20 km to the northwest of Hashir Crater, Duvolo Crater exposes some olivine-bearing material underlying Fe/Mg-smectite-bearing materials in its crater wall (Figures 8, 14, and 15). This may seem inconsistent with the stratigraphy elsewhere in Libya Montes; however, given the inversion of stratigraphy as a consequence of the formation of crater ejecta [e.g., *Melosh*, 1989] and the observation that these two units occur within the crater-wall/rim

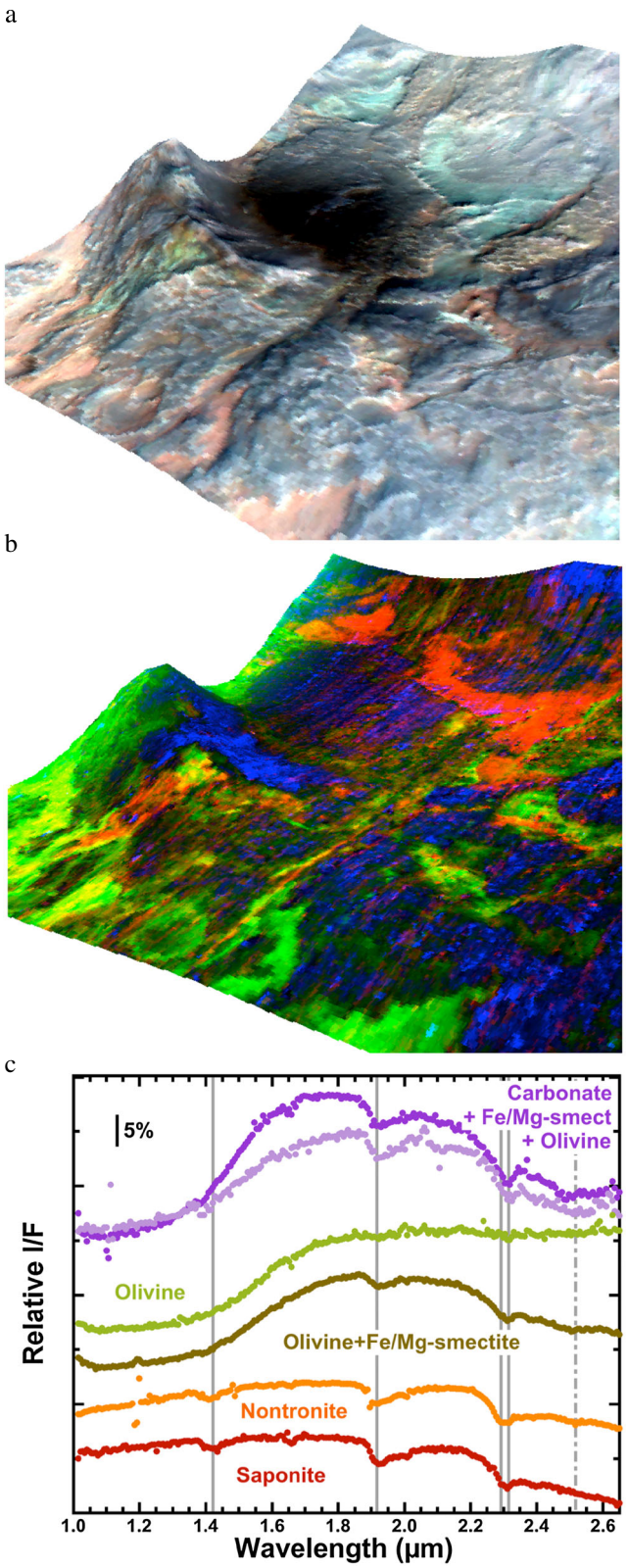

Figure 12. CRISM image FRT00018800 south of Duvolo Crater in the central phyllosilicate outcrop: (a) 3D image view prepared with R 2500 nm, G 1500 nm, B 1208 nm, 5× vertical exaggeration; (b) 3D image view prepared with R D2300, G OLINDEX, B LCP parameters, 5× vertical exaggeration; and (c) ratioed *I*/*F* spectra from 1.04–2.65 μm with a 5% band depth scale bar.

of Duvolo, the crater-inverted stratigraphy is therefore consistent with the general stratigraphy of the region (i.e., olivine-rich unit overlies the smectite-rich unit in the pre-Duvolo-impact target). Essentially Duvolo Crater, in contrast to Hashir Crater, formed after the emplacement of the olivine-bearing unit. Targeted CRISM image FRT0000CE72 captures the mineralogy of the eastern portion of Duvolo Crater. Mineralogy maps and spectra are shown in Figure 14 for this image. 3D CRISM images are displayed in Figure 15 that show relationships among the mineralogically distinct units. The morphology of the units is illustrated in Figure 16. In the crater wall/rim of Duvolo Crater crudely layered olivine-rich materials (bluish) are overlain by an Fe/Mg-smectite-bearing unit (yellowish) (Figure 16b). The morphologies of the beidellite-bearing unit (eroding terrace block) in the lower crater wall of Duvolo is shown in Figure 16c and of the saponite-bearing unit which correlates with materials eroding out of the crater wall in Figure 16d. These units were likely excavated from the pre-impact target, but impact induced alteration cannot be ruled out.

[42] The largest outcrop of phyllosilicate-bearing units captured by CRISM targeted images in Libya Montes to date is located north of Hashir Crater (Figures 9–11) and east of Duvolo Crater (Figures 8, 14–16). Targeted CRISM image FRT000A819 features the mineralogy of the Libya Montes region. Mineralogy maps and spectra are shown in Figure 17 for this image. Analyses of the spectra in this image indicate the presence of pyroxene- and olivine-bearing units as in other regions. Variability is observed in the spectral features of the Fe/Mg-smectite unit such that regions more typical of nontronite (spectral bands at 1.43, 1.91, 2.29, 2.40 μm) and more typical of saponite (spectral bands at 1.40, 1.91, 2.31, 2.39 μm) are observed. In some regions an increase in depth of the 2.5 μm absorption indicative of carbonate, chlorite, and/or serpentine is present together with the Fe/Mg-smectite bands. The spectral shape and wavelength position of this feature is more consistent with carbonate in most cases. These units also exhibit an olivine band suggesting that regions containing carbonate are mixtures of carbonate, smectite and olivine. An Al-smectite is also observed in a few small bright deposits. This is identified as beidellite by spectral features at 1.41, 1.91, and 2.19 μm, which are distinguishable from the 1.41, 1.91, and 2.20–2.21 μm bands characteristic of montmorillonite, another Al-smectite.

[43] Newly available hyperspectral analyses were tested on preliminary versions of the MTRDR form of image FRT000A819 as well. Selected results of the end-member analyses are shown in Figure 18. This algorithm identified spectra having relative differences in the band strengths near 1.9 and 2.3 μm. The spectra characterized by stronger bands near 1.9 μm are associated with Fe/Mg-smectite from the spectral ratio analyses (Figure 17). The spectra having stronger bands at 2.3 μm correlated well with the spectra that also exhibited a band near 2.5 μm (Figure 18). The detections with stronger bands near 2.3 and 2.5 μm are consistent with regions identified from the spectral ratio analyses with carbonate-like spectral signatures. The spectra having bands near 2.5 μm were further divided into those with band centers ≤2.53 μm (red, Figure 18b) and those with band centers >2.53 μm (blue, Figure 18b). Dolomite has a

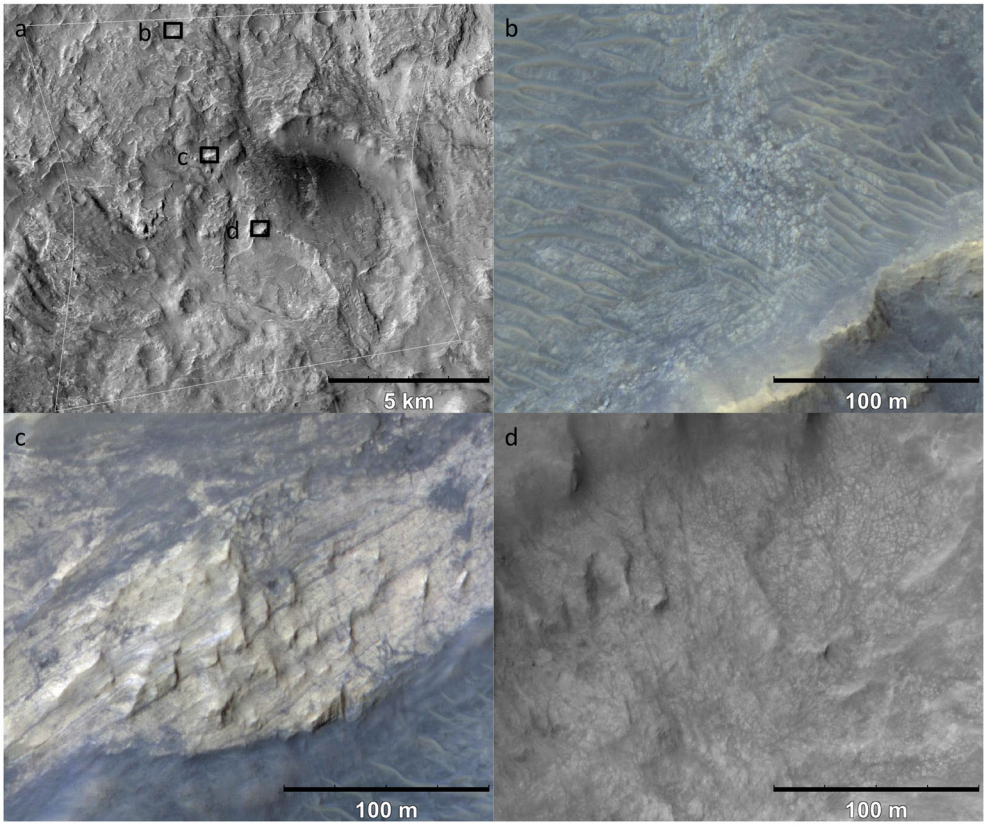

Figure 13. Morphology from CTX and HiRISE of the units shown in Figure 12: (a) CTX image B22_018368_1824 showing outline of CRISM image FRT00018800 and sites of HiRISE views all taken from ESP_017656_1835, (b) olivine-rich region from HiRISE IRB image, (c) bright-toned Fe/Mg-smectite-bearing unit, and (d) Fe/Mg-smectite-bearing unit.

band center at 2.52 μm and magnesite has a band center at 2.50 μm. The red regions correspond to sites consistent with carbonate-like features using the ratio analysis technique (Figure 17). The blue regions with bands at wavelengths longer than 2.53 μm are correlated well with the Fe/Mg-smectite detections for regions having stronger bands at 1.9 μm compared to 2.3 μm (green, Figure 18a).

[44] The results of the tetracorder analyses are shown in Figure 19. These analyses found a ferrous-bearing basalt matched well with the regions identified as an olivine-bearing unit from the spectral ratio analyses. The tetracorder analyses found a good match with nontronite (but not for saponite) for the regions characterized as Fe/Mg-smectite from the spectral ratio analyses and for the regions defined as having stronger bands near 1.9 μm than 2.3 μm (Figure 19), which correspond to the green regions in Figure 18a. The tetracorder analyses found matches with both a chlorite-serpentine-bearing rock and dolomite for a third region identified as having a band near 2.5 μm (Figure 19). The shape of this 2.5 μm band is highly variable with differences in the band center and bandwidth. In general the tetracorder analyses showed a better match with the chlorite-serpentine-bearing rock than the dolomite. No other carbonate minerals were detected. The band near 3.3–3.5 μm was also not identified in the tetracorder analyses in relation to the other features observed, which indicates that carbonates are not spectrally dominant phases. The regions exhibiting a band near 2.5 μm were generally identified as olivine and nontronite as well as chlorite-serpentine /dolomite, indicating a mixture of these components is likely present.

[45] Figure 20 shows a CTX view of the region around CRISM image FRT0000A819 and expanded HiRISE views of the morphology of several units. HiRISE analyses indicate differences in the surface morphologies for the surface outcrops spectrally dominated by phyllosilicate, olivine, and pyroxene. The beidellite-rich materials occur on the relatively steep slopes of the massif (~33 degrees over ~440 m) as light-toned materials that appear to be eroding out of massifs that are common in the Libya Montes region (Figure 20c). These massifs, mapped by various workers as Noachian-aged materials [*Greeley and Guest*, 1986; *Crumpler and Tanaka*, 2003; *Tanaka et al*., 2005] and generally mapped by OMEGA and CRISM as pyroxene-bearing material, likely represent ancient basaltic crustal materials that predate but were subsequently modified by the Isidis Basin-forming event. Whether or not the conditions that prevailed postbasin or prebasin contributed to the alteration that gave rise to the beidellite-rich materials cannot be easily determined.

[46] Layering and polygonal fractures are observed in this region for the olivine-bearing unit (not shown) but are similar to olivine-bearing morphology observed elsewhere

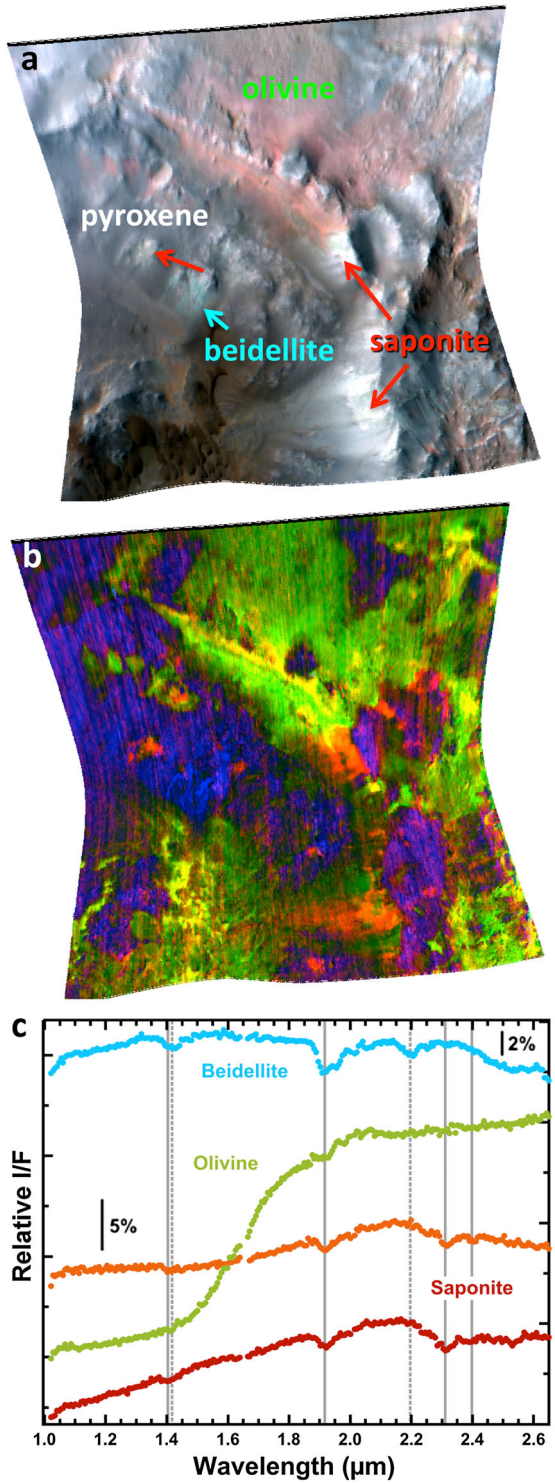

Figure 14. CRISM image FRT0000CE72 of Duvolo crater rim in the central phyllosilicate outcrop: (a) FRT0000CE72 prepared with R 2529 nm, G 1506 nm, B 1080 nm with olivine-bearing regions in red, pyroxene-bearing regions in gray, saponite-bearing outcrops marked by red arrows, and the beidellite-rich outcrop labeled with a blue arrow. (b) FRT0000CE72 prepared with R D2300, G OLINDEX, B LCP parameters. (c) Ratioed *I*/*F* spectra 1.04–2.65 μm from FRT0000CE72 with a 2% band depth scale bar for the beidellite-type spectrum and a 5% band depth scale bar for the other spectra.

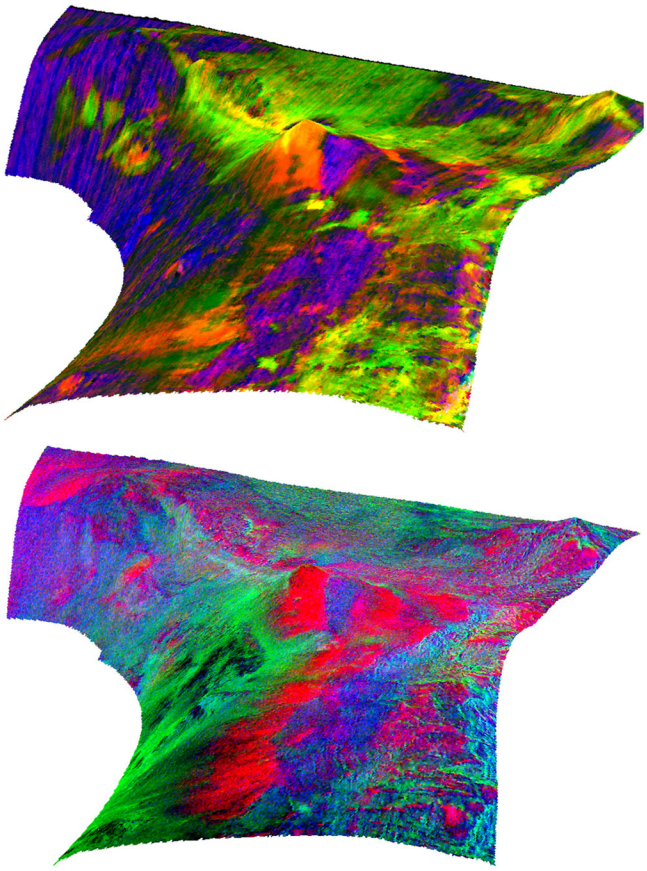

Figure 15. 3D view of CRISM image FRT0000CE72 draped over MOLA elevations (5× vertical enhancement). N is left and image is ~12 km wide. (a) Prepared with R D2300, G OLINDEX, B LCP parameters. (b) Prepared with R BD530, G BDI1000VIS, B SH600.

in the region (e.g., Figures 9b and 11). The region exhibiting carbonate-like features in addition to Fe/Mg-smectite and olivine signatures in CRISM image FRT0000A819 has abundant polygonal cracking features (Figure 20d). What appears to be folded alternating layered materials, possibly foliation based on its appearance (Figure 20b), correlates with the saponite-rich materials. It is uncertain whether the putative foliation is the source of the strongest of the saponite-signature. A small light-toned outcrop with a polygonal texture (and possibly fractures) correlates with the nontronite-rich materials (Figure 20e). The regions bearing saponite-like and nontronite-like spectral signatures are largely similar in CRISM image FRT0000A819 and are probably altered regions of the ancient massif bedrock that experienced slight variations in fluid chemistry during the time of alteration.

[47] Three-dimensional CRISM images are shown in Figure 21 that illustrate the stratigraphy of the units. The olivine-bearing unit (red) unconformably overlies the Fe/Mg-smectite-bearing unit (gray-cyan) and the olivine-bearing unit appears to be eroded back in several regions revealing the ancient phyllosilicate-bearing unit. The pyroxene-bearing massifs rise up toward the east of CRISM image FRT0000A819. The bright beidellite patch can be seen on the flanks of the massif. Figure 21b shows how the

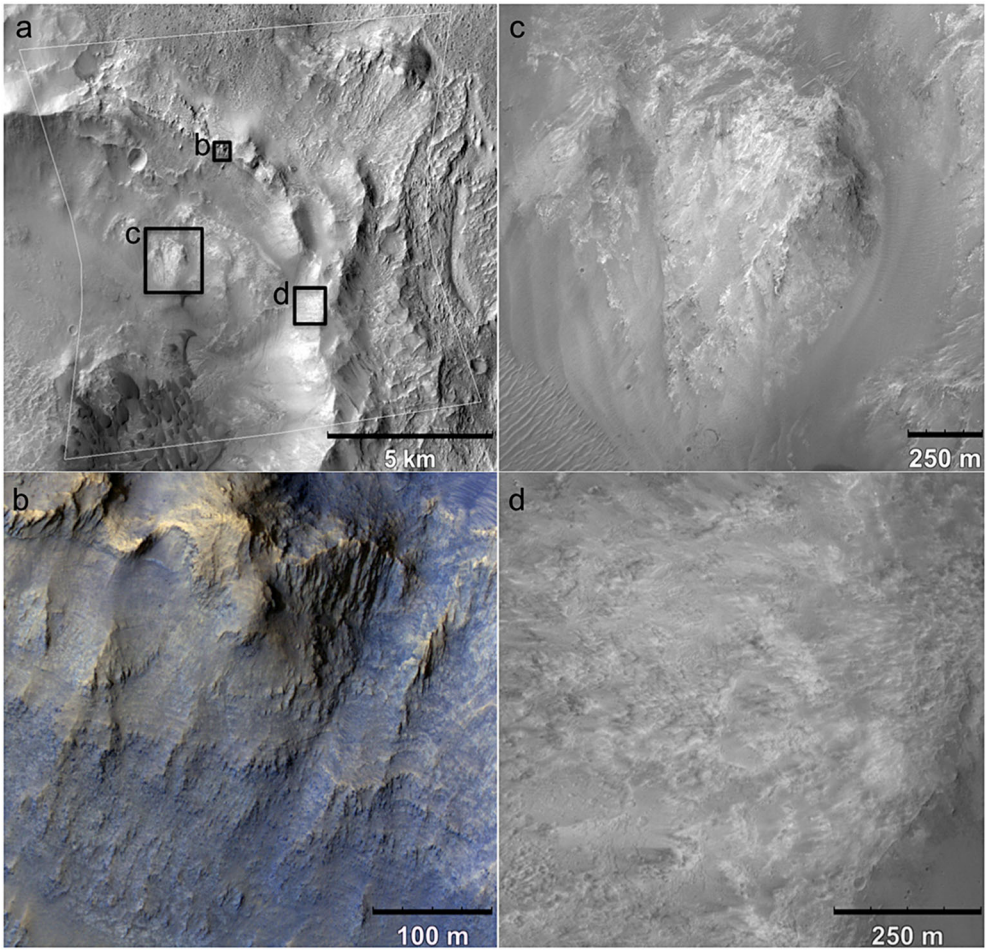

Figure 16. Morphology from CTX and HiRISE of the units shown in Figure 14. (a) View of CTX image B20_017445_1835_XN_03N275W showing the northeast portion of Duvolo Crater covered by FRT0000CE72. (b) Possible inverted stratigraphy in the crater wall/rim of Duvolo Crater showing crudely layered olivine-rich materials (bluish) overlain by a Fe/Mg-smectite-bearing unit (yellowish) in HiRISE image ESP_019357_1835. (c) Close-up of the beidellite-bearing unit (eroding terrace block) in the lower crater wall of Duvolo. (d) Close-up of saponite-bearing unit which correlates with materials eroding out of the crater wall.

olivine-rich unit is draped over the topography, suggesting an airfall origin, perhaps welded pyroclastics or impact melt [*Mustard et al*., 2009], or lava flows [*Tornabene et al*., 2008]. See also the 3D movie (auxiliary materials) of these images for additional views.

[48] Views from the HiRISE DTM colored using CRISM mineralogy are shown in Figure 22. The olivine-bearing unit is shown in green, the Fe/Mg-smectite-bearing unit in pink, and the pyroxene-bearing unit in blue. Where the olivine unit appears thin and eroded a mixture of olivine and Fe/Mg-smectite is observed (yellow). This can be seen in a small outcrop of layered bedrock in the center of Figure 22a and much of Figure 22b. The outcrop (Figure 22a) also exhibits polygonal cracking that is characteristic of olivine for this region; however, the polygonal cracks are most clearly visible at the base of the olivine-bearing unit where the spectra contain signatures of Fe/Mg-smectite as well as olivine. The widespread yellow region exhibiting polygonal cracking in Figure 22b has spectral signatures consistent with Fe/Mg-smectite, carbonate and olivine. This is likely an outcrop of the Fe/Mg-smectite-rich unit that altered to form carbonate and contains or is covered by a small amount of the olivine that did not erode or alter.

3.3. Detailed Spectral Analyses

[49] CRISM spectra of several typical units in the Libya Montes region are shown in Figure 23. There are many regions with distinct olivine signatures (e.g., spectra #1, 2, Figure 23a) as well as a few spots spectrally dominated by olivine that also contain weak pyroxene signatures (e.g., spectrum #4, Figure 23a). The Feuerbach sample contains olivine and augite and shares some similarities to this type of material. The tetracorder analyses for CRISM image FRT000A819 showed a better correlation for an olivine-bearing rock with this material than for either olivine or pyroxene (augite) minerals, indicating that this unit is likely an olivine-bearing basalt with additional components. The olivine-bearing spectra at Libya Montes are more consistent

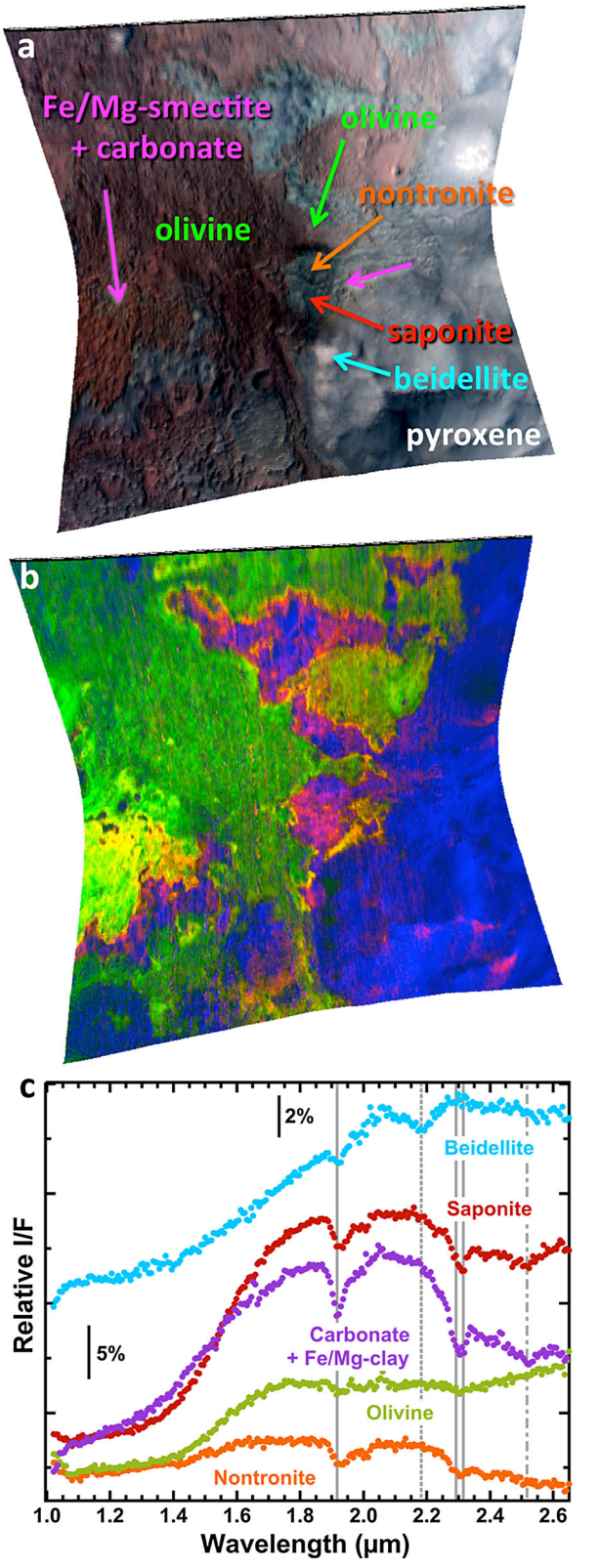

Figure 17. CRISM image FRT0000A819 at the central phyllosilicate outcrop: (a) prepared with R 2529 nm, G 1506 nm, B 1080 nm, (b) prepared with R D2300, G OLINDEX, B LCP parameters, (c) ratioed *I/F* spectra 1.04–2.65 μm with a 2% band depth scale bar for the beidellite-type spectrum and a 5% band depth scale bar for the other spectra.

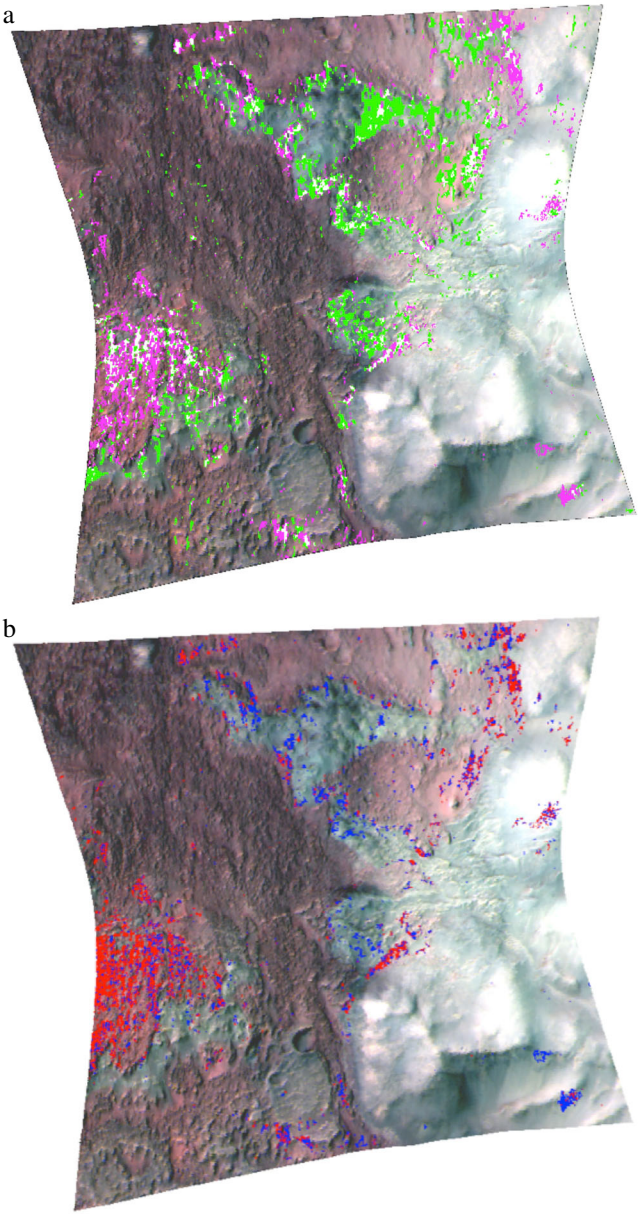

Figure 18. Results of end-member analyses for CRISM image FRT0000A819 (note that these are performed on the nongeoreferenced images and results are georeferenced and overlayed on the standard CRISM IR product): (a) Spectra with a stronger 1.9 μm band and weaker 2.3 μm band (green) are compared to spectra with a weaker 1.9 μm band and stronger 2.3 μm band (pink). (b) Spectra exhibiting a band near 2.5 μm are divided into band centers ≤2.53 μm (red) and >2.53 μm (blue).

with lab spectra of coarse grains or chips than with spectra of fine particulate samples. This indicates that the olivine-dominated materials are likely rock units and in-place regolith rather than fine-grained mobile silt/sand. Some olivine-dominated sites also contain a hydration band near 1.9 μm indicative of alteration (e.g., spectrum #3, Figure 23a). This supports the idea that the olivine unit has been altered and eroded in some regions. In places the olivine-bearing unit appears sufficiently thin to allow the lower Fe/Mg-

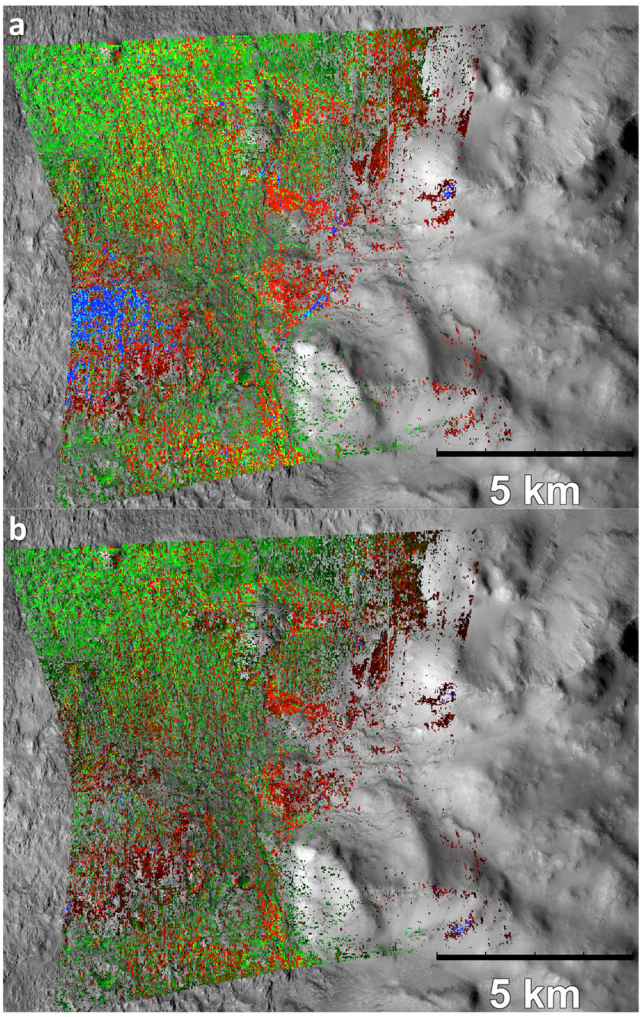

Figure 19. Mineral maps from Tetracorder analyses of CRISM image FRT0000A819 overlain on CTX (P05_002822_1822): (a) R nontronite, G ferrous basalt, and B chlorite-serpentine-bearing rock, and (b) R nontronite, G ferrous basalt, and B dolomite. The chlorite-serpentine and dolomite occurrences appear in similar locations, but the chlorite-serpentine-bearing rock provided a better match and exhibited higher abundances for this analysis.

smectite-bearing unit to protrude; however, these spectra look different (contain bands near 1.9, 2.3, and sometimes 2.5 μm). The olivine plus 1.9 μm band spectral signature indicates that the olivine itself has been altered in some regions to form a hydrated component rather than that the olivine-bearing unit has simply been physically eroded to become thinner and allow spatial mixing with exposed phyllosilicate-bearing units below it.

[50] Small bright patches of material are observed shedding off the massif in CRISM image FRT0000A819 (Figure 21) that contain spectral features near 1.40, 1.92, and 2.19 μm (Figures 17 and 23b). The spectral signature is more consistent with the Al-smectite beidellite than montmorillonite. Beidellite typically forms at higher temperatures than montmorillonite or could be the result of hydrothermal alteration or burial diagenesis [e.g., *Bishop et al*., 2011; *Guisseau et al*., 2007]. The band near 2.19 μm is broad which could be consistent with a mixture of some allophane as well; however, beidellite is more consistent with the observed spectral features. Allophane is a nanophase aluminosilicate indicative of young volcanic soils [e.g., *Parfitt et al*., 1980] and its spectral properties have been reported recently [*Bishop et al*.,]. Small bright outcrops have been observed toward the east of Libya Montes in fluvial-looking features [*Bishop et al*., 2010; *Erkeling et al*., 2012] that are also spectrally consistent with beidellite [*Bishop et al*., 2011].

[51] The most dominant phyllosilicate is Fe/Mg-smectite (Figure 23c). This is observed in the lower unit where the olivine is eroded back in several CRISM images throughout the Libya Montes region. The spectra contain features near 1.91–1.92 and 2.29–2.31 μm. The Fe-bearing nontronite end-member exhibits this OH combination band near 2.28–2.29 μm, while it is observed closer to 2.31 μm for saponite [e.g., *Bishop et al*., 2008b]. In some cases the OH stretching overtone is observed near 1.4 μm. This is observed near 1.42–1.43 μm for nontronite and near 1.38–1.39 μm for Mg-phyllosilicates [*King and Clark*, 1989; *Bishop et al*., 2008a]. Additional bands are also observed near 2.38 μm for Mg-smectites (saponite/hectorite), near 2.41 μm for nontronite and near 2.40 μm for Fe/Mg-smectite [e.g., *Bishop et al*., 2008b]. Variations in these spectral features across the Libya Montes region indicate that the Fe and Mg abundance in the smectite is variable; however, tetracorder analyses indicated a greater consistency with nontronite than with saponite.

[52] In a few less common regions, additional bands are also observed near 2.52 and 3.42–3.50 μm for this Fe/Mg-smectite-bearing unit (Figures 23c and 23d). Spectral features are observed near 2.5 μm for Mg-rich phyllosilicates such as chlorite and serpentine [*King and Clark*, 1989; *Bishop et al*., 2008a] and also for carbonates [*Clark et al*., 1990; *Wagner and Schade*, 1996; *Ehlmann et al*., 2008]. Tetracorder analyses indicated better matches to a chlorite-serpentine rock than to a carbonate for these regions (Figure 19). The feature observed near 3.42–3.50 μm is most consistent with the carbonate dolomite, but was not observed to correlate with these regions in the tetracorder analyses. The intensity of this band near 3.4–3.5 μm is well correlated with the intensity of the 2.52 μm band in spectra ratioed by hand (e.g., Figures 17 and 23c). These unique areas also contain a ferrous slope consistent with olivine or siderite (Fe^{2+}-carbonate). Olivine is more likely to be the cause of this feature as the bands near 2.3, 2.5, and 3.4 μm do not correlate as well with those of siderite as with those of dolomite. A definitive carbonate type is difficult to identify due to spectral mixing effects [*Bishop et al*., 2011]. This nontronite-magnesite mixture study showed that large amounts of carbonate were needed to shift the band center from 2.28–2.29 μm observed for nontronite toward 2.30–2.31 μm observed for magnesite, which could indicate that if carbonates are mixed with Fe/Mg-smectite on Mars they could be difficult to detect at low abundance using this band. This study also found that only small amounts of olivine (~10 wt %) are needed in mixtures with nontronite and magnesite to contribute greatly toward the ferrous slope.

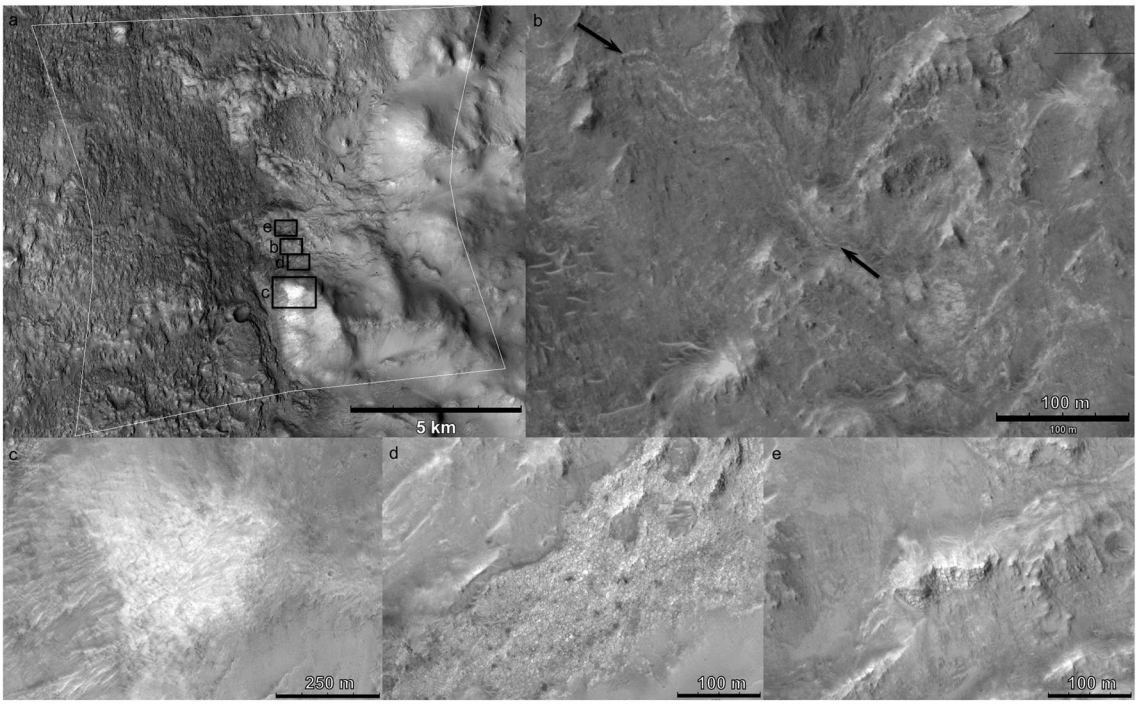

Figure 20. Morphology from CTX and HiRISE of the units shown in Figure 17. (a) CTX image P05_002822_1822 with an outline of FRT0000A819, (b) close-up of saponite-bearing unit in HiRISE image ESP_016034_1835 exhibiting what appears to be possible folding or foliation bands (arrows), (c) close-up of beidellite-rich unit, (d) close-up of Fe/Mg-smectite + carbonate + olivine unit, and (e) close-up of nontronite-bearing unit.

4. Discussion

[53] Understanding the ages of surface units and their intercorrelations is essential to constraining chemical processes such as the formation of phyllosilicates. Libya Montes is one of the oldest regions on Mars that shows evidence of extensive impact and volcanic activity as well as aeolian and fluvial erosion over most of Martian geologic history [*Scott and Tanaka*, 1986; *Crumpler and Tanaka*, 2003; *Erkeling et al*., 2010; *Jaumann et al*., 2010]. Analysis of the spectral data and geologic mapping indicate that the phyllosilicate alteration products are correlated with the ancient Noachian bedrock (unit Nm). The Fe/Mg-rich phyllosilicates are detected in many sites throughout the Libya Montes region and are most commonly associated with craters, ridges, and massifs where the olivine-rich unit was not emplaced or has since been eroded. This suggests that a detectable portion of the ancient basalt may have altered to Fe/Mg-phyllosilicates, likely under near-neutral conditions. Less common are bright patches of Al-phyllosilicates that appear to be a result of chemical alteration of the ancient basalt in localized regions. Because these are altered from the same ancient basalt, it is possible that the conditions at the time of formation were more acidic to enable leaching of the Fe and Mg and crystallization of Al-phyllosilicate, although sulfates were not observed. Outcrops of phyllosilicates are most abundant in the central Libya Montes region, but smaller outcrops are also present in the western and eastern Libya Montes region. The olivine and pyroxene signatures are strongest in the western to central portion of the region in OMEGA and CRISM map tile images. The eastern region has a lower thermal inertia and contains a high level of dust that may be partially masking the surface mineralogy.

[54] The observations of this study support a scenario for the development of the Libya Montes region that includes alteration of ancient basaltic crust, followed by emplacement of an olivine-rich unit and then emplacement of a pyroxene-bearing basaltic caprock (Figure 24). Olivine-bearing terrains are well correlated with the high thermal inertia unit (unit HAe) [*Murphy et al*., 2007; *Tornabene et al*., 2008] and are interpreted to be lava flows exhibiting hummocky and rough texture, which are positioned under the smoother pyroxene-bearing lava flows forming the caprock, consistent with the work of *Tornabene et al*. [2008]. The Libya Montes likely consist of crust that was uplifted and faulted as a consequence of the formation of the Isidis Basin. In addition to these adjustments of the crust in response to the formation of the basin, impact ejecta and melts would have been emplaced at this time. The crust and these materials may be represented by the NHf unit (Figure 2), although the region is heavily modified and extensively dissected. Thus, remnants of former Isidis ejecta might long since have been removed or reworked by fluvial processes or covered by the lava flows deposited during the multiple phases of volcanic activity of Syrtis and Tyrrhena.

[55] Alteration of the ancient basalt at Libya Montes and formation of the mountains are likely associated with the

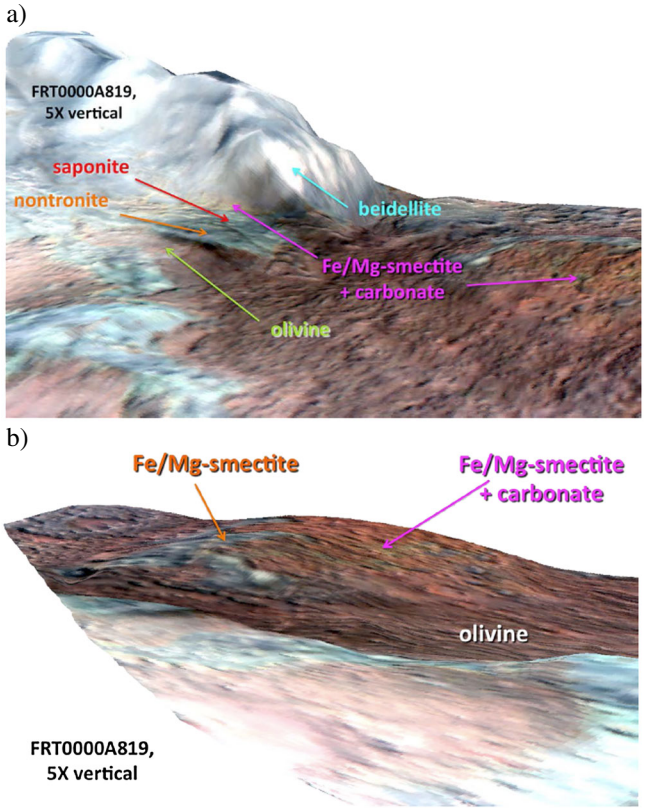

Figure 21. 3D view of CRISM image FRT0000A819 draped over MOLA elevations with 5× vertical enhancement. (a) NE is up and image is ~8 km wide and (b) SE is up and image is ~5 km wide.

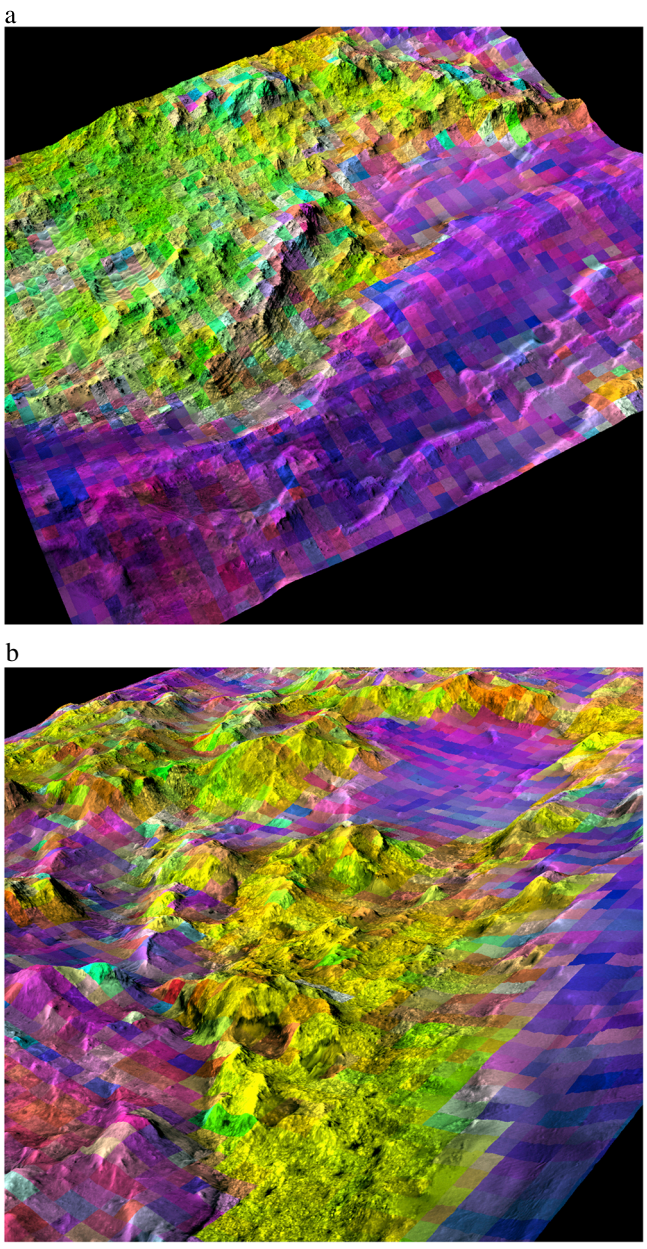

Figure 22. 3D perspective images of the CRISM FRT0000A819 site (see Figures 17–21). These images were generated by combining a CRISM spectral summary parameter color image with an orthorectified HiRISE red mosaic image (DT2EA_016034_1835_017089_1835_A01), which is draped over a HiRISE stereo-derived DTM (DTEEC_016034_1835_017089_1835_A01) with a 3× vertical enhancement. Fe/Mg-smectite is shown in pink, olivine in green, and pyroxene in blue: (a) Olivine-rich layers embaying and superposing altered basaltic rocks. (b) Fe/Mg-smectite + carbonate + olivine unit (yellow-orange).

Isidis impact, which is estimated at ~4 Ga [*Werner*, 2008]. Alteration of the bedrock to form Fe/Mg-rich phyllosilicates in some regions is likely to have been a long-term process and may have continued to take place after the montes were formed. The phyllosilicate formation could have been subsurface as suggested by *Ehlmann et al.* [2011] or at the surface and associated with Noachian aged terrains containing fluvial features. In either case, heat caused by the Isidis impact is likely to have mobilized liquid water from melting subsurface ice in the regolith that would have contributed toward alteration of the basalt and formation of the Fe/Mg-rich phyllosilicates. Views of the ancient basaltic rocks along crater rims (e.g., Hashir Crater) and other exposures show that both unaltered basalt and basalts containing Fe/Mg-smectite are present in the lowest unit. This supports partial alteration of this ancient bedrock and variations in the Fe/Mg ratios and variations in additional phyllosilicates or aqueous phases associated with the Fe/Mg-smectite, rather than a homogeneous alteration unit. The bulk of the Fe/Mg-rich phyllosilicate material is most consistent with nontronite, but smaller regions are present that are more consistent with saponite. Other regions were found where dolomite, chlorite and/or serpentine appear to be mixed with the Fe/Mg-smectite, although no outcrops were found having spectral signatures dominated by carbonate. This unit appears to occur just below the surface of the olivine—e.g., where the olivine-bearing unit is thinned out or worn through in small locations. A possible explanation for the Fe/Mg-smectite/carbonate/olivine mixture is that carbonate coexists with the Fe/Mg-smectite in the altered regions of the ancient basalt, but that the carbonate is less stable and is scoured off the surface faster than the smectite when exposed below the

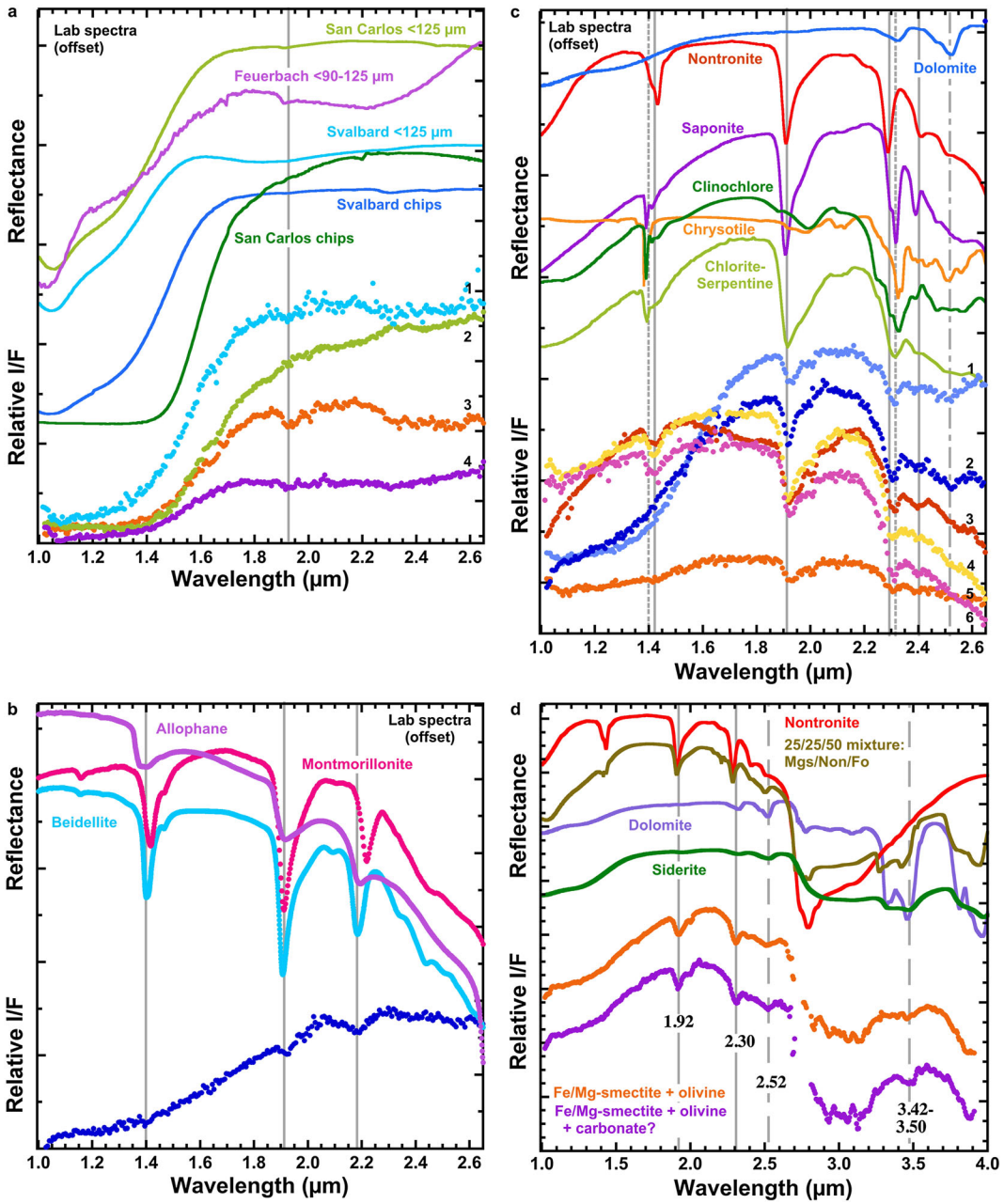

Figure 23. Selected ratioed CRISM *I/F* spectra from nongeoreferenced images in Libya Montes for comparison with lab spectra: (a) Olivine-bearing regions. Spectrum #1: FRT00018800 *x*492*y*312/*x*492*y*273 10×10, spectrum #2: FRT0000A909 *x*235*y*360/*x*235*y*385 5×5, spectrum #3: FRT0000A819 *x*330*y*80/*x*330*y*89 3×3, spectrum #4: FRT0000A819 *x*270*y*230/*x*270*y*78 5×5. Lab spectra: San Carlos forsterite [*Bishop et al.*, 2011], olivine-rich rock from Svalbard (from D. Blake), olivine-bearing basalt from Feuerbach [*Harloff and Arnold*, 2001; *Bishop et al.*, 2002]. (b) Bright patch of beidellite-bearing material on massif in FRT000A819 at *x*286*y*97/*x*286*y*54 3×3. Lab spectra: montmorillonite [*Bishop et al.*, 2008a], beidellite [*Bishop et al.*, 2011], allophane. (c) Fe/Mg-smectite-bearing regions. CRISM spectrum #1: FRT0000A819 *x*270*y*130/*x*270*y*78 5×5, spectrum #2: FRT0000A819 *x*568*y*176/*x*568*y*359 3×3, spectrum #3: FRT000047D8 *x*168*y*94/*x*168*y*189 10×10, spectrum #4: FRT0000A909 *x*393*y*195/*x*393*y*107 5×5, spectrum #10 FRT0000A819 *x*270*y*184/*x*270*y*78 5×5. Lab spectra: chlorite-serpentine-bearing rock and saponite [*Clark et al.*, 2007], other phyllosilicates [*Bishop et al.*, 2008a], dolomite [*Bishop et al.*, 1998], dolomite and siderite [*Bishop et al.*, 1998]. (d) Likely carbonate-bearing regions from FRT000A819 at *x*568*y*174/*x*568*y*294 10×10 and *x*567*y*167/*x*567*y*380. Lab spectra: nontronite [*Bishop et al.*, 2008a], mixture [*Bishop et al.*, 2011].

olivine. The carbonate could also be forming at the base of the olivine-rich unit (transition of unit Nm/NHf to HAe) where heat from either an impact melt or lava flow could have further altered the phyllosilicate-bearing basalt.

[56] Small, bright deposits were also observed in a few locations in the ancient basaltic rocks of the Libya Montes containing the Al-smectite beidellite. These appear to be unrelated to the Fe/Mg-phyllosilicate regions and could have formed at a later date, although a pre-Isidis formation cannot be ruled out. Unfortunately, these are too small and too few to determine if they are older or more recent than the olivine-rich unit. Beidellite forms at elevated temperatures compared to another Al-smectite montmorillonite, and beidellite is typically associated with hydrothermal processes or burial diagenesis [e.g., Guisseau *et al*., 2007].

[57] Figure 25 illustrates the general stratigraphy understood for the region as exhibited in central Libya Montes as well as the stratigraphy at Hashir Crater, which punctured the massif material and was later partially filled with olivine. The olivine unit is cut by the more recent craters, but covers over the crater rims for older ones such as Hashir Crater. The olivine-bearing terrains could have formed through emplacement of primitive picritic lavas originating from Syrtis Major or the southern highlands following the formation of Isidis Basin [*Tornabene et al*., 2008], or from impact melts created and emplaced as a consequence of the Isidis basin-forming event [*Mustard et al*., 2007], or they could be a nearly globally distributed layer deposited by a mega-impact event [*Edwards and Christensen*, 2011] or they could be olivine-rich pyroclastics similar to those observed in Gusev Crater [*Squyres et al*., 2007]. The pyroxene-bearing caprock (units HAvod and HAe, depending on the degree of aeolian erosion) was formed by lava flows emanating from Syrtis Major that infiltrated the basin and part of the highlands from the west and southwest [e.g., *Tornabene et al*., 2008].

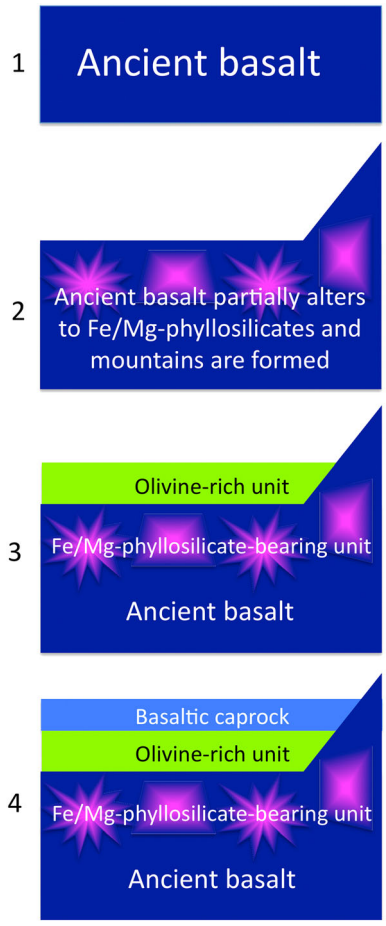

Figure 24. Diagram of possible formation scenario for major units at Libya Montes.

5. Summary and Conclusions

[58] A commonly occurring stratigraphy in the Libya Montes region consists of an ancient basalt unit, covered by an olivine-rich unit and topped by the pyroxene-bearing caprock. The ancient basalt has been partially altered to form Fe/Mg-smectite in many locations, and to Fe/Mg-smectite plus other Fe/Mg-bearing phyllosilicates and/or the carbonate dolomite in a few small locations. The carbonate-like signatures are always observed together with spectral features due to Fe/Mg-smectite and olivine. These ancient phyllosilicate-bearing units are observed most clearly in the region surrounding Hashir and Duvolo Craters in central Libya Montes. These aqueously-formed materials likely developed through chemical alteration and hydrothermal activity preceding and resulting from the formation of the Isidis Basin, and may have been further modified by the pervasive fluvial activity throughout this region. Fe/Mg-smectite-bearing units are frequently characterized by layering and polygonal fracturing in HiRISE images. However, these are also characteristic of the olivine-bearing units at the same scale.

[59] The Al-smectite beidellite is observed as small, bright patches that appear to be eroding out of the flanks of a massif (e.g., Duvolo Crater, Figure 14 and north of Hashir Crater, Figure 21) or associated with fluvial features [e.g., *Bishop et al*., 2010]. It may have formed subsequently to the Fe/Mg-smectite-bearing material and exhibits a different morphology, but occurs together with the same ancient basalt unit. Thus, the beidellite must have formed under different aqueous conditions, possibly indicating hydrothermal processes.

[60] Libya Montes is one of the most geologically diverse regions on Mars, where surface rocks date from the Noachian to the Amazonian and there is ample evidence of ancient fluvial activity and chemical alteration. The mountains are composed of the Noachian basalt, which was partially altered to phyllosilicates. Variations in the composition of the aqueous materials may be due to subsequent alteration over time.

[61] **Acknowledgments.** The authors are grateful to the science and operations teams from MRO CRISM and HiRISE, Mars Express OMEGA and HRSC for acquiring the data. Support to several team members from the MRO project and a NASA-PGG grant are much appreciated. This research has also been partially supported by the research alliance "Planetary Evolution and Life." Thanks are also due to E. Cloutis and J. Michalski for helpful reviews and to NASA's PGG program and Lunar Science Institute for supporting Brown University's RELAB facility.

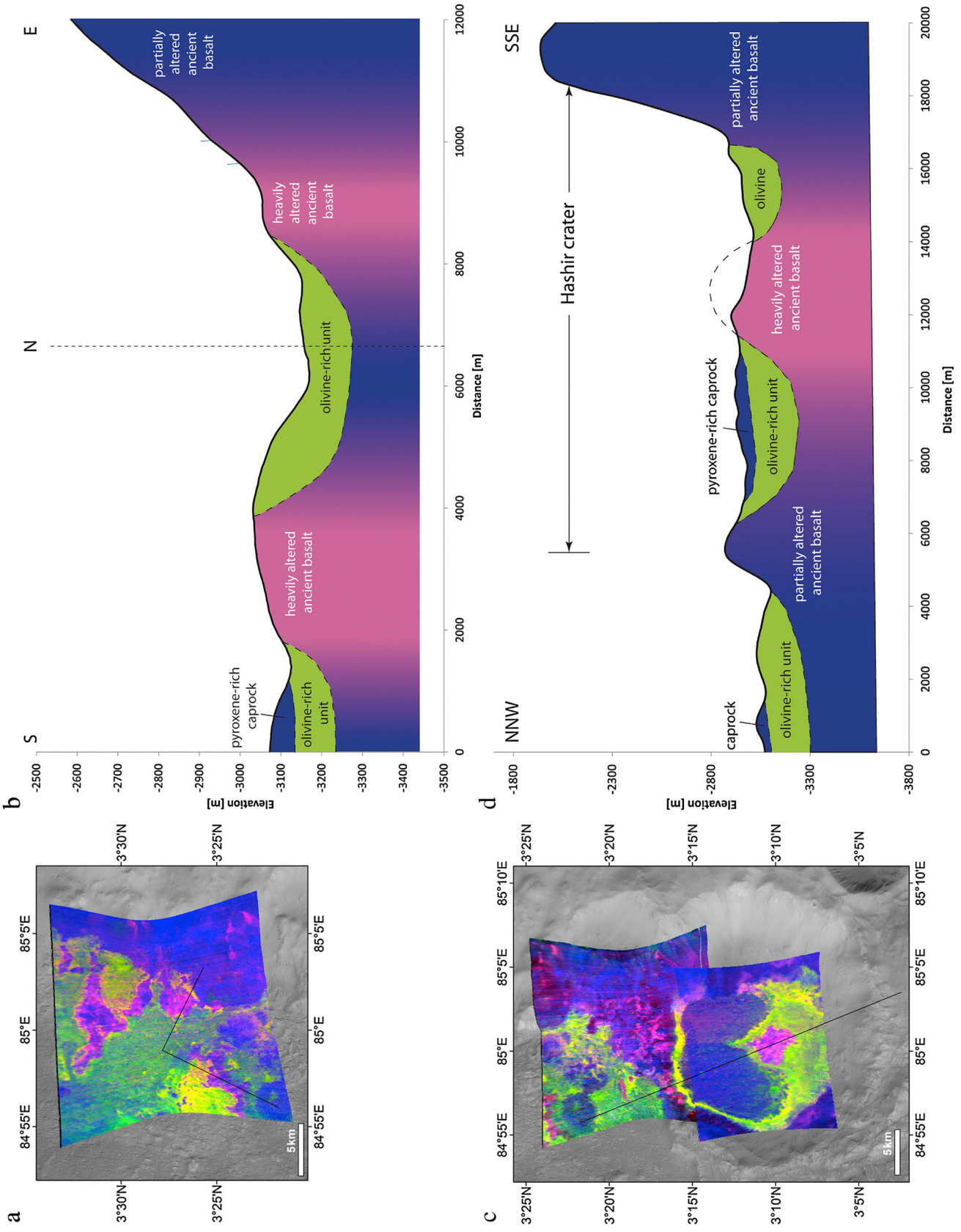

Figure 25. Stratigraphy of major units at Libya Montes: (a) transect across pyroxene-bearing caprock, olivine-rich basalt, phyllosilicate-bearing altered basalt and partially altered basalt captured in CRISM image FRT0000A819, (b) stratigraphy profile for region shown in Figure 25a, (c) transect across Hashir Crater from CRISM images FRT000047D8 and FRT0001647D, (d) stratigraphy at Hashir Crater.

References

Bamberg, M., R. Jaumann, and H. Asche (2012), Floor Fractured Craters Around Syrtis Major, Mars, paper presented at Lunar Planet Science Conf., The Woodlands, TX.

Bibring, J.-P., Y. Langevin, A. Gendrin, B. Gondet, F. Poulet, M. Berthé, A. Soufflot, R. Arvidson, N. Mangold, J. Mustard, and P. Drossart (2005), Mars surface diversity as revealed by the OMEGA/Mars Express observations, *Science*, *307*(11March 2005), 1576–1581.

Bishop, J. L., J. F. Mustard, C. M. Pieters, and T. Hiroi (1998), Recognition of minor constituents in reflectance spectra of ALH 84001 chips and the importance for remote sensing on Mars, *Meteor. Planet. Sci.*, *33*, 693–698.

Bishop, J. L., C. M. Pieters, M. D. Dyar, V. E. Hamilton, and J. Harloff (2002), A spectral, chemical and mineralogical study of Mars analogue rocks, paper presented at Lunar Planet. Sci. XXXIII., Lunar Planet. Inst., Houston.

Bishop, J. L., M. D. Lane, M. D. Dyar, and A. J. Brown (2008a), Reflectance and emission spectroscopy study of four groups of phyllosilicates: Smectites, kaolinite-serpentines, chlorites and micas, *Clay Miner.*, *43*, 35–54.

Bishop, J. L., E. Z. Noe Dobrea, N. K. McKeown, M. Parente, B. L. Ehlmann, J. R. Michalski, R. E. Milliken, F. Poulet, G. A. Swayze, J. F. Mustard, S. L. Murchie, and J.-P. Bibring. (2008b), Phyllosilicate diversity and past aqueous activity revealed at Mawrth Vallis, Mars, *Science*, *321*(5890, 8 August 2008), 1159830–1159833, doi:10.1126/science.1159699.

Bishop, J. L., H. D. Makarewicz, K. A. Perry, N. K. McKeown, M. Parente, L. L. Tornabene, G. A. Swayze, R. N. Clark, J. F. Mustard, S. L. Murchie, and A. S. McEwen (2010), Mineralogy of the Libya Montes and the Southern Isidis Planitia region: CRISM detection of clay, carbonate, olivine and pyroxene, and correlation with HiRISE imagery, paper presented at Lunar Planet. Sci. Conf., LPI, The Woodlands, TX.

Bishop, J. L., W. P. Gates, H. D. Makarewicz, N. K. McKeown, and T. Hiroi (2011), Reflectance spectroscopy of beidellites and their importance for Mars, *Clays Clay Miner.*, *59*(4), 376–397.

Bishop, J. L., E. B. Rampe, L. L. Baker, D. L. Bish, A. Abidin, T. Henmi, and S. Hillier (2011), Character of short-range ordered aluminosilicates and their possible presence on Mars, paper presented at 48th Annual Meeting of The Clay Minerals Society, *J. Geophys. Res.*, p. 31, September 24–29.

Burns, R. G. (1993), *Mineralogical Applications of Crystal Field Theory*. 2nd Edition, pp. 551, Cambridge University Press, Cambridge, UK.

Clark, R. N., T. V. V. King, M. Klejwa, and G. A. Swayze (1990), High spectral resolution reflectance spectroscopy of minerals, *J. Geophys. Res.*, *95*(B8), 12653–12680.

Clark, R. N., G. A. Swayze, K. E. Livo, R. F. Kokaly, S. J. Sutley, J. B. Dalton, R. R. McDougal, and C. A. Gent (2003a), Imaging spectroscopy: Earth and planetary remote sensing with the USGS Tetracorder and expert systems, *J. Geophys. Res.*, *108*(E12), 5131, doi:5110.1029/2002JE001847.

Clark, R. N., G. A. Swayze, R. Wise, E. Livo, T. Hoefen, R. Kokaly, and S. J. Sutley (2003b), USGS digital spectral library splib05a: U.S. Geological Survey Open-File Report 03-395, http://pubs.usgs.gov/of/2003/ofr-2003-2395 pp, U.S. Geological Survey.

Clark, R. N., G. A. Swayze, R. Wise, E. Livo, T. Hoefen, R. Kokaly, and S. J. Sutley (2007), USGS digital spectral library splib06a, U.S. Geological Survey.

Crumpler, L. (2012), Mars landing sites in phyllosilicate, carbonate, and ancient wet Noachian terrains of Libya Montes, paper presented at 43rd Lunar Planet. Sci. Conf., The Woodlands, TX.

Crumpler, L. S., and K. L. Tanaka (2003), Geology and the MER target site characteristics along the southern rim of Isidis Planitia, Mars, *J. Geophys. Res.*, *108*(E12), 8080, doi:8010.1029/2002JE002040.

Delamere, W. A., L. L. Tornabene, A. S. McEwen, K. Becker, J. W. Bergstrom, N. T. Bridges, E. M. Eliason, D. Gallagher, K. E. Herkenhoff, L. Keszthelyi, S. Mattson, G. K. McArthur, M. T. Mellon, M. Milazzo, P. S. Russell, and N. Thomas (2010), Color imaging of Mars by the High Resolution Imaging Science Experiment (HiRISE), *Icarus*, *205*(1), 38–52.

Edwards, C. S., and P. R. Christensen (2011), Evidence for a Widespread Olivine-Rich Layer on Mars: Identification of a Global Impact Ejecta Deposit?, paper presented at 42nd Lunar Planet. Sci. Conf., The Woodlands, TX.

Ehlmann, B. L., J. F. Mustard, S. L. Murchie, F. Poulet, J. L. Bishop, A. J. Brown, W. M. Calvin, R. N. Clark, D. J. Des Marais, R. E. Milliken, L. H. Roach, T. L. Roush, G. A. Swayze, and J. J. Wray (2008), Oribtal identification of carbonate-bearing rocks on Mars, *Science*, *322*(19 December 2008), 1828–1832.

Ehlmann, B. L., J. F. Mustard, G. A. Swayze, R. N. Clark, J. L. Bishop, F. Poulet, D. J. D. Marais, L. H. Roach, R. E. Milliken, J. J. Wray, O. Barnouin-Jha, and S. L. Murchie (2009), Identification of hydrated silicate minerals on Mars using MRO-CRISM: Geologic context near Nili Fossae and implications for aqueous alteration, *J. Geophys. Res.*, *114*(CRISM special issue), doi:10.1029/2009JE003339.

Ehlmann, B. L., J. F. Mustard, S. L. Murchie, J. P. Bibring, A. Meunier, A. A. Fraeman, and Y. Langevin (2011), Subsurface water and clay mineral formation during the early history of Mars, *Nature*, *479*, 53–60.

Erkeling, G., D. Reiss, H. Hiesinger, and R. Jaumann (2010), Morphologic, stratigraphic and morphometric investigations of valley networks in eastern Libya Montes, Mars: Implications for the Noachian/Hesperian climate change, *Earth Planet. Sci. Lett.*, *294*, 291–305.

Erkeling, G., D. Reiss, H. Hiesinger, F. Poulet, J. Carter, M. A. Ivanov, E. Hauber, and R. Jaumann (2012), Valleys, paleolakes and possible shorelines at the Libya Montes / Isidis boundary: Implications for the hydrologic evolution of Mars, *Icarus*, *219*(1), 393–413.

Gillespie, A. R., A. B. Kahle, and R. E. Walker (1986), Color enhancement of highly correlated images. I. Decorrelation and HSI contrast stretches. *Remote Sens. Environ.*, *20*(3), 209–235.

Greeley, R., and J. E. Guest (1986), Geologic map of the eastern equitorial region of Mars, Map I-1802-B, U.S. Geol. Surv., Flagstaff, AZ.

Guisseau, D., P. P. Mas, D. Beaufort, J. P. Girard, A. Inoue, B. Sanjuan, S. Petit, A. Lens, and A. Genter (2007), Significance of the depth-related transition montmorillonite-beidellite in the Bouillante geothermal field, (Guadeloupe, Lesser Antilles) *Am. Mineral.*, *92*(11–12), 1800–1813.

Gwinner, K., F. Scholten, M. Spiegel, R. Schmidt, B. Giese, J. Oberst, C. Heipke, R. Jaumann, and G. Neukum (2009), Derivation and Validation of High-Resolution Digital Terrain Models from Mars Express HRSC Data, *Photogramm. Eng. Rem. Sens.*, *75*(9), 1127–1142.

Hamilton, V. E., and P. R. Christensen (2005), Evidence for extensive, olivine-rich bedrock on Mars, *Geology*, *33*(6), 433–436.

Harloff, J., and G. Arnold (2001), Near-infared reflectance spectroscopy of bulk analog materials for planetary crust, *Planet. Space Sci.*, *49*, 191–211.

Hartmann, W. K., and G. Neukum (2001), Cratering chronology and the evolution of Mars, (Guadeloupe, Lesser Antilles) *Space Sci. Rev.*, *96*, 165–194.

Hoefen, T. M., R. N. Clark, J. L. Bandfield, M. D. Smith, J. C. Pearl, and P. R. Christensen (2003), Discovery of olivine in the Nili Fossae region of Mars, *Science*, *302*(24 October), 627–630.

Irwin, R. P., R. A. Craddock, and A. D. Howard (2005), Interior channels in Martian valley networks: Discharge and runoff production, *Geology*, *33* (6), 489–492, doi:410.1130/g21333.21331.

Ivanov, B. A. (2001), Mars/Moon cratering rate ratio estimates, *Chronology and Evolution of Mars*, *96*, 87–104.

Ivanov, M. A., H. Hiesinger, G. Erkeling, F. J. Hielscher, and D. Reiss (2012), Major episodes of geologic history of Isidis Planitia on Mars, *Icarus*, *218*(1), 24–46.

Jaumann, R., S. Reiss, G. Frei, G. Neukum, F. Scholten, K. Gwinner, T. Roatsch, K. D. Matz, V. Mertens, E. Hauber, H. Hoffmann, U. Köhler, J. W. Head, H. Hiesinger, and M. H. Carr (2005), Interior channels in Martian valleys: Constraints on fluvial erosion by measurements of the Mars Express High Resolution Stereo Camera, *Geophys. Res. Lett.*, *32*, 16203–16210. doi:11029/12005GL023415.

Jaumann, R., G. Neukum, T. Behnke, T. C. Duxburry, K. Eichentopf, S. van Gasselt, B. Giese, K. Gwinner, E. Hauber, H. Hoffmann, A. Hoffmeister, U. Köhler, K.-D. Matz, T. B. McCord, V. Mertens, J. Oberst, R. Pischl, D. Reiss, E. Ress, T. Roatsch, P. Saiger, F. Scholten, G. Schwarz, K. Stephan, M. Wählisch, and t. HRSC Co-Investigator and Experiment Team (2007), The High Resolution Stereo Camera (HRSC) Experiment on Mars Express: Instrument aspects and experiment conduct from interplanetary cruise through nominal mission, *Planet. Space Sci.*, *55*, 928–952.

Jaumann, R., A. Nass, D. Tirsch, D. Reiss, and G. Neukum (2010), The Western Libya Montes Valley System on Mars: Evidence for episodic and multi-genetic erosion events during the Martian history, *Earth Planet. Sci. Lett.*, *294*, 272–290.

King, T. V. V., and R. N. Clark (1989), Spectral characteristics of chlorites and Mg-serpentines using high-resolution reflectance spectroscopy, *J. Geophys. Res.*, *94*(B10), 13,997–914,008.

Kirk, R. L., E. Howington-Kraus, M. R. Rosiek, J. A. Anderson, B. A. Archinal, K. J. Becker, D. A. Cook, D. M. Galuszka, P. E. Geissler, T. M. Hare, I. M. Holmberg, L. P. Keszthelyi, B. L. Redding, W. A. Delamere, D. Gallagher, J. D. Chapel, E. M. Eliason, R. King, and A. S. McEwen (2008), Ultrahigh resolution topographic mapping of Mars with MRO HiRISE stereo images: Meter-scale slopes of candidate Phoenix landing sites, *J. Geophys. Res.*, *113*(E12), E00A24, doi:10.1029/2007JE003000.

Kneissl, T., S. van Gasselt, and G. Neukum (2011), Map-projection-independent crater size-frequency determination in GIS environments--New software tool for ArcGIS, *Planet. Space Sci*, *59*(11-12), 1243–1254, doi:1210.1016/j.pss.2010.1203.1015.

Malaret, E. R., C. D. Hash, S. L. Murchie, P. C. McGuire, R. E. Arvidson, M. J. Wolff, M. D. Smith, S. M. Pelkey, T. Z. Martin, A. McGovern, F. P.

Seelos, T. Choo, D. C. Humm, W.-J. Shyong, and C. Team (2008), Construction of the CRISM Global Multispectral Map of Mars, paper presented at 39th Lunar Planet. Sci. Conf., League City, TX.

Malin, M. C., J. F. Bell III, B. A. Cantor, M. A. Caplinger, W. M. Calvin, R. T. Clancy, K. S. Edgett, L. Edwards, R. M. Haberle, P. B. James, S. W. Lee, M. A. Ravine, P. C. Thomas, and M. J. Wolff (2007), Context Camera Investigation on board the Mars Reconnaissance Orbiter, *J. Geophys. Res.*, *112*, E05S04, doi:10.1029/2006JE002808.

Malin, M. C., K. S. Edgett, B. A. Cantor, M. A. Caplinger, G. E. Danielson, E. H. Jensen, M. A. Ravine, J. L. Sandoval, and K. D. Supulver (2010), An overview of the 1985-2006 Mars Orbiter Camera science investigation, *Mars*, *5*, 1–60.

McEwen, A. S., et al. (2010), The High Resolution Imaging Science Experiment (HiRISE) during MRO's Primary Science Phase (PSP), *Icarus*, *205* (1), 2–37 doi:10.1016/j.icarus.2009.1004.1023.

McGuire, P. C., M. J. Wolff, M. D. Smith, R. E. Arvidson, S. L. Murchie, R. T. Clancy, T. L. Roush, S. C. Cull, K. A. Lichtenberg, S. M. Wiseman, R. O. Green, T. Z. Martin, R. E. Milliken, P. J. Cavendar, D. C. Humm, F. P. Seelos, K. D. Seelos, H. W. Taylor, B. L. Ehlmann, J. F. Mustard, S. M. Pelkey, T. N. Titus, C. D. Hash, E. R. Malaret, and C. Team (2008), MRO/CRISM Retrieval of Surface Lambert Albedos for Multispectral Mapping of Mars with DISORT-based Radiative Transfer Modeling: Phase 1 -- Using Historical Climatology for Temperatures, Aerosol Optical Depths, and Atmospheric Pressures, *Trans. Geosci. Rem. Sens.*, *46*(12), 4020–4040.

McGuire, P. C., J. L. Bishop, A. J. Brown, A. A. Fraeman, G. A. Marzo, M. F. Morgan, S. L. Murchie, J. F. Mustard, M. Parente, S. M. Pelkey, T. L. Roush, F. P. Seelos, M. D. Smith, L. Wendt, and M. J. Wolff (2009), An improvement to the volcano-scan algorithm for atmospheric correction of CRISM and OMEGA spectral data, *Planet. Space. Sci.*, *57* (7), 809–815.

Melosh, M. H. (1989), *Impact Cratering: A Geologic Process*, 245 pp., Oxford University Press, New York.

Michael, G., and G. Neukum (2010), Planetary surface dating from crater size-frequency distribution measurements: Partial resurfacing events and statistical age uncertainty, *Earth Planet. Sci. Lett.*, *294*, 2233–2229, doi:2210.1016/j.epsl.2009.2212.2041.

Michael, G. G., T. Platz, T. Kneissl, and N. Schmedemann (2012), Planetary surface dating from crater size–frequency distribution measurements: Spatial randomness and clustering, *Icarus*, *218*(1), 169–177.

Murchie, S., et al. (2007), Compact Reconnaissance Imaging Spectrometer for Mars (CRISM) on Mars Reconnaissance Orbiter (MRO), *J. Geophys. Res.*, *112*(E05S03), doi:10.1029/2006JE002682.

Murchie, S. L., F. P. Seelos, C. D. Hash, D. C. Humm, E. Malaret, J. A. McGovern, T. H. Choo, K. D. Seelos, D. L. Buczkowski, M. F. Morgan, O. S. Barnouin-Jha, H. Nair, H. W. Taylor, G. W. Patterson, C. A. Harvel, J. F. Mustard, R. E. Arvidson, P. McGuire, M. D. Smith, M. J. Wolff, T. N. Titus, J.-P. Bibring, and F. Poulet (2009), The Compact Reconnaissance Imaging Spectrometer for Mars investigation and data set from the Mars Reconnaissance Orbiter's primary science phase, *J. Geophys. Res.*, *114*(CRISM special issue), doi:10.1029/2009JE003344.

Murphy, N. W., B. M. Jakosky, S. C. Rafkin, K. W. Larsen, N. E. Putzig, and M. T. Mellon (2007), Thermophysical properties of the Isidis basin, Mars, *J. Geophys. Res.*, *112*, E05004 05001-05031.

Mustard, J., F. Poulet, J. W. Head, N. Mangold, J.-P. Bibring, S. M. Pelkey, C. Fassett, Y. Langevin, and G. Neukum (2007), Mineralogy of the Nili Fossae region with OMEGA/Mars Express data: 1. Ancient impact melt in the Isidis Basin and implications for the transition from the Noachian to Hesperian, *J. Geophys. Res.*, *112*(E08SO3), doi:10.1029/2006JE002834.

Mustard, J. F., B. L. Ehlmann, S. L. Murchie, F. Poulet, N. Mangold, J. W. Head, J.-P. Bibring, and L. H. Roach (2009), Composition, morphology, and stratigraphy of Noachian crust around the Isidis basin, *J. Geophys. Res.*, *114*(CRISM special issue), doi:10.1029/2009JE003349.

Neukum, G. (2007), Meteoritenbombardement und Datierung planetarer Oberflächen, (Guadeloupe, Lesser Antilles) *Hablilitation Thesis*, 186 pp., Ludwig-Maximilians-Universität: München, Germany.

Neukum, G., and K. Hiller(1981), Martian ages, *J. Geophys. Res.*, *86*, 3097–3121.

Neukum, G., R. Jaumann, and t. HRSC Co-Investigator and Experiment Team (2004), HRSC: The High Resolution Stereo Camera of Mars Express, in *Mars Express: The Scientific Payload*, edited by A. Wilson, pp. 17–35, ESA, Noordwijk, The Netherlands.

Ody, A., F. Poulet, J.-P. Bibring, D. Loizeau, B. Gondet, Y. Langevin, and J. F. Mustard (2013), Global investigation of olivine on Mars: insights into crust and mantle compositions, *J. Geophys. Res.*, submitted.

Ody, A., F. Poulet, Y. Langevin, J.-P. Bibring, G. Bellucci, F. Altieri, B. Gondet, M. Vincendon, and J. Carter (2012), Global anhydrous mineral maps of the surface of Mars from OMEGA/Mex after seven years of observations, *J. Geophys. Res.*, *118*, doi: 10.1029/2012JE004149.

Parente, M. (2008), A new approach to denoising CRISM images, paper presented at Lunar Planet. Sci. Conf., LPI, Houston, TX.

Parente, M., J. F. Mustard, S. L. Murchie, and F. P. Seelos (2011), Robust unmixing of hyperspectral images: Application to Mars, paper presented at IEEE International Geoscience and Remote Sensing Symposium, IGARSS 2011, Vancouver, BC, Canada, July 24-29, 2011.

Parfitt, R. L., R. J. Furkert, and T. Henmi (1980), Identification and structure of two types of allophane from volcanic ash soils and tephra, *Clays Clay Miner.*, *28*(5), 328–334.

Pelkey, S. M., J. F. Mustard, S. Murchie, R. T. Clancy, M. Wolff, M. Smith, R. E. Milliken, J.-P. Bibring, A. Gendrin, F. Poulet, Y. Langevin, and B. Gondet (2007), CRISM multispectral summary products: Parameterizing mineral diversity on Mars from reflectance, *J. Geophys. Res.*, *112* (E08S14), doi:10.1029/2006JE002831.

Perry, K. A., J. L. Bishop, M. D. Dyar, D. F. Blake, S. Peel, and A. J. Brown (2011), Spectral analysis of nontronite-magnesite-olivine mixtures and implications for carbonates on Mars, paper presented at Lunar Planet. Sci. Conf., XLII Abstract 1554.

Pinet, P. C., F. Heuripeau, H. Clenet, S. Chevrel, Y. Daydou, D. Baratoux, C. Rosemberg, J.-P. Bibring, F. Poulet, B. Gondet, J. F. Mustard, S. LeMouélic, and G. Bellucci (2007), Mafic mineralogy variations across Syrtis Major shield and surroundings as inferred from visible-near-infrared spectroscopy by OMEGA/Mars Express, paper presented at 7th Int'l Mars Conf., Pasadena.

Poulet, F., C. Gomez, J.-P. Bibring, Y. Langevin, B. Gondet, P. Pinet, G. Belluci, and J. F. Mustard (2007), Martian surface mineralogy from Observatoire pour la Minéralogie, l'Eau, les Glaces et l'Activité on board the Mars Express spacecraft (OMEGA/MEx): Global mineral maps, *J. Geophys. Res.*, *112*(E08S02), doi:10.1029/2006JE002840.

Scholten, F., K. Gwinner, T. Roatsch, K. D. Matz, M. Wählisch, B. Giese, J. Oberst, R. Jaumann, G. Neukum, and H. C. Team (2005), Mars Express HRSC Data Processing - Methods and Operational Aspects, *Photogramm. Eng. Rem. Sens.*, *71*(10), 1143–1152.

Scott, D. H., and K. L. Tanaka (1986), Geologic map of the western equatorial region of Mars, USGS Misc., Invest. Ser. Map I-1802-A, 1:15000000 scale, U.S. Geol. Surv., Reston, VA.

Seelos, F. P. (2011), CRISM data processing and analysis products update - calibration, correction, and visualization, paper presented at 42nd Lunar Planet. Sci. Conf., The Woodlands, TX.

Seelos, F. P., M. F. Morgan, H. W. Taylor, S. L. Murchie, D. C. Humm, K. D. Seelos, O. S. Barnouin, C. E. Viviano, and CRISMTeam (2012), CRISM Map Projected Targeted Reduced Data Records (MTRDRs) – High Level Analysis and Visualization Data Products, paper presented at Planetary Data: A Workshop for Users and Software Developers, Flagstaff, AZ.

Skok, J. R., J. F. Mustard, S. L. Murchie, M. B. Wyatt, and B. L. Ehlmann (2010), Spectrally distinct ejecta in Syrtis Major, Mars: Evidence for environmental change at the Hesperian-Amazonian boundary, *J. Geophys. Res.*, *115*(E00D14), doi:10.1029/2009JE003338.

Squyres, S. W., O. Aharonson, B. C. Clark, B. A. Cohen, L. Crumpler, P. A. DeSouza, W. H. Farrand, R. Gellert, J. Grant, J. P. Grotzinger, A. F. C. Haldemann, J. R. Johnson, G. Klingelhöfer, K. W. Lewis, R. Li, T. McCoy, A. S. McEwen, H. Y. McSween, D. W. Ming, J. M. Moore, R. V. Morris, T. J. Parker, J. W. Rice, Jr., S. Ruff, M. Schmidt, C. Schröder, L. A. Soderblom, and A. Yen (2007), Pyroclastic Activity at Home Plate in Gusev Crater, Mars, *Science*, *316*, 738–742.

Tanaka, K. L., D. H. Scott, and R. Greeley (1992), Global stratigraphy (Ch. 11), in *Mars*, edited by H. H. Kieffer, et al., pp. 345–382, Univ. of Arizona Press, Tucson.

Tanaka, K. L., J. A. Skinner Jr., and T. M. Hare (2005), Geologic map of the Northern Plains of Mars, Map 2888, U.S. Geol. Surv., Flagstaff, AZ.

Tornabene, L. L., J. E. Moersch, H. Y. McSween, V. E. Hamilton, J. L. Piatek, and P. R. Christensen (2008), Surface and crater-exposed lithologic units of the Isidis Basin as mapped by coanalysis of THEMIS andd TES derived data products, *J. Geophys. Res.*, *113*(E10001), doi:10.1029/2007JE002988.

Wagner, C., and U. Schade (1996), Measurements and Calculations for Estimating the Spectrometric Detection Limit for Carbonates in Martian Soil, *Icarus*, *123*(2), 256–268.

Werner, S. C. (2005), *Major aspects of the chrono-stratigraphy and geologic evolutionary history of Mars*, Freie Universitaet Berlin, Berlin.

Werner, S. C. (2008), The early martian evolution - Constraints from basin formation ages, *Icarus*, *195*(1), 45–60.

Wichman, R. W., and P. H. Schultz (1989), Sequence and Mechanisms of Deformation Around the Hellas and Isidis Impact Basins on Mars, *J. Geophys. Res.*, *94*(B12), 17,333–317,357.